



AFRL-RY-WP-TR-2011-1309

**DIODE-PUMPED, 2-MICRON, Q-SWITCHED
THULIUM:Y₃Al₅O₁₂ (Tm:YAG) MICROCHIP LASER**

Charles D. Phelps

University of Dayton

MAY 2011

Interim Report

Approved for public release; distribution unlimited.

See additional restrictions described on inside pages

STINFO COPY

**AIR FORCE RESEARCH LABORATORY
SENSORS DIRECTORATE
WRIGHT-PATTERSON AIR FORCE BASE, OH 45433-7320
AIR FORCE MATERIEL COMMAND
UNITED STATES AIR FORCE**

NOTICE AND SIGNATURE PAGE

Using Government drawings, specifications, or other data included in this document for any purpose other than Government procurement does not in any way obligate the U.S. Government. The fact that the Government formulated or supplied the drawings, specifications, or other data does not license the holder or any other person or corporation; or convey any rights or permission to manufacture, use, or sell any patented invention that may relate to them.

This report was cleared for public release by the USAF 88th Air Base Wing (88 ABW) Public Affairs Office (PAO) and is available to the general public, including foreign nationals. Copies may be obtained from the Defense Technical Information Center (DTIC) (<http://www.dtic.mil>).

AFRL-RY-WP-TR-2011-1309 HAS BEEN REVIEWED AND IS APPROVED FOR PUBLICATION IN ACCORDANCE WITH ASSIGNED DISTRIBUTION STATEMENT.

*//Signature//

PATRICK A. BERRY
Work Unit Manager
EO Countermeasures Technology Branch
Multispectral Sensing & Detection Division

//Signature//

JOHN F. CARR, Chief
EO Countermeasures Technology Branch
Multispectral Sensing & Detection Division

//Signature//

TRACY W. JOHNSTON, Chief
Multispectral Sensing & Detection Division
Sensors Directorate

This report is published in the interest of scientific and technical information exchange, and its publication does not constitute the Government's approval or disapproval of its ideas or findings.

*Disseminated copies will show “//Signature//” stamped or typed above the signature blocks.

REPORT DOCUMENTATION PAGE				Form Approved OMB No. 0704-0188	
<p>The public reporting burden for this collection of information is estimated to average 1 hour per response, including the time for reviewing instructions, searching existing data sources, gathering and maintaining the data needed, and completing and reviewing the collection of information. Send comments regarding this burden estimate or any other aspect of this collection of information, including suggestions for reducing this burden, to Department of Defense, Washington Headquarters Services, Directorate for Information Operations and Reports (0704-0188), 1215 Jefferson Davis Highway, Suite 1204, Arlington, VA 22202-4302. Respondents should be aware that notwithstanding any other provision of law, no person shall be subject to any penalty for failing to comply with a collection of information if it does not display a currently valid OMB control number. PLEASE DO NOT RETURN YOUR FORM TO THE ABOVE ADDRESS.</p>					
1. REPORT DATE (DD-MM-YY) May 2011		2. REPORT TYPE Interim		3. DATES COVERED (From - To) 17 June 2008 – 07 May 2011	
4. TITLE AND SUBTITLE DIODE-PUMPED, 2-MICRON, Q-SWITCHED THULIUM:Y ₃ Al ₅ O ₁₂ (Tm:YAG) MICROCHIP LASER				5a. CONTRACT NUMBER In-house	
				5b. GRANT NUMBER	
				5c. PROGRAM ELEMENT NUMBER 62204F	
6. AUTHOR(S) Charles D. Phelps				5d. PROJECT NUMBER 2003	
				5e. TASK NUMBER 13	
				5f. WORK UNIT NUMBER 20031135	
7. PERFORMING ORGANIZATION NAME(S) AND ADDRESS(ES) University of Dayton 300 College Park Avenue Dayton, OH 45469				8. PERFORMING ORGANIZATION REPORT NUMBER	
9. SPONSORING/MONITORING AGENCY NAME(S) AND ADDRESS(ES) Air Force Research Laboratory Sensors Directorate Wright-Patterson Air Force Base, OH 45433-7320 Air Force Materiel Command United States Air Force				10. SPONSORING/MONITORING AGENCY ACRONYM(S) AFRL/RMWA	
				11. SPONSORING/MONITORING AGENCY REPORT NUMBER(S) AFRL-RY-WP-TR-2011-1309	
12. DISTRIBUTION/AVAILABILITY STATEMENT Approved for public release; distribution unlimited.					
13. SUPPLEMENTARY NOTES PAO Case Number: 88ABW-11-3282.; Clearance Date: 08 Jun 2011. This report, which is a thesis in partial fulfillment of the requirements for a Master of Science in Electro-optics, contains color.					
14. ABSTRACT <p>In this report we discuss the design, simulation, construction, and characterization of an actively Q-switched, diode-pumped solid state laser operating at 2 μm. The laser cavity has a “microchip” configuration and uses a 6% thulium-doped YAG crystal as the lasing medium. In continuous wave mode, we achieve output powers of up to 450 mW with a slope efficiency of 9.5%. Using an acousto-optic Q-switch, the laser was run in pulsed mode at an average power of 42 mW and a pulse rate of 1.66 kHz. Pulse duration was approximately 400 ns with a pulse energy of 25 μJ. The center wavelength was 2.019 μm with a line width of ≤0.045 nm.</p> <p>Additionally, a design is presented for replacing the active Q-switch with a chromium-doped zinc selenide crystal acting as a saturable absorber passive Q-switch. Finally, we will propose possible future modifications to the laser system design to improve its performance, ruggedness and compactness, and to broaden its functionality.</p>					
15. SUBJECT TERMS					
16. SECURITY CLASSIFICATION OF:			17. LIMITATION OF ABSTRACT: SAR	18. NUMBER OF PAGES 84	19a. NAME OF RESPONSIBLE PERSON (Monitor) Patrick A. Berry 19b. TELEPHONE NUMBER (Include Area Code) N/A
a. REPORT Unclassified	b. ABSTRACT Unclassified	c. THIS PAGE Unclassified			

TABLE OF CONTENTS

Section	Page
LIST OF ILLUSTRATIONS	iii
LIST OF TABLES	vi
ACKNOWLEDGEMENTS	vii
CHAPTER 1 – INTRODUCTION	1
1.1 Motivation.....	1
1.2 Overview of Thesis.....	4
CHAPTER 2 – MATERIAL CHARACTERIZATION	6
2.1 Energy Level Structure.....	6
2.2 Laser Transitions.....	7
2.3 YAG	14
2.4 Production	14
2.5 Material Data.....	15
CHAPTER 3 – LASER SYSTEM DESIGN	17
3.1 Overview of Design Objectives	17
3.2 Mirrors	18
3.3 Pump Sources.....	20
3.4 Lasing Medium	27
3.5 Thermal Lens	33
3.6 Active Q-Switch.....	34
3.7 Heat Sinks.....	35
3.8 Final System Design	37
CHAPTER 4 – PASSIVE Q-SWITCHING.....	39
4.1 Background	39
4.2 Design.....	40
4.3 Modeling	42
CHAPTER 5 – LASER PERFORMANCE AND CHARACTERIZATION	46
5.1 First Attempt and Subsequent Thermal Damage	46
5.2 Output Power and Slope Efficiency	47
5.3 Findlay-Clay Analysis	49
5.4 Spectral Content	50
5.5 Beam Profiling.....	52
5.6 Pulsed Performance.....	52
CHAPTER 6 – CONCLUSIONS AND DISCUSSION	54
6.1 Conclusions.....	54
6.2 Future Work	54
REFERENCES	56
APPENDIX A – RATE EQUATION MODELING	58
APPENDIX B – ADDITIONAL CALCULATIONS	62
B.1 Peak Power of a Gaussian Pulse.....	62
B.2 Estimating Beam Quality	62
B.3 Calculating Absorption Coefficient for Tm:YAG.....	63
B.4 Absorption with Compensation for Fresnel Reflectance.....	64

TABLE OF CONTENTS (CONCL.)

Section	Page
APPENDIX C – MATLAB CODE	65
C.1 Cr:ZnSe/Cr:ZnS Passive Q-Switch Model.....	65
C.2 Tm:YAG Laser Model – Parameter Definitions	66
C.3 Tm:YAG Laser Model – Differential Equation Solver	69

LIST OF ILLUSTRATIONS

Figure	Page
Figure 1: Incident (blue) and reflected (red) signals, with dispersion, for a hypothetical laser radar system. Note that in the case of the longer pulses, there is significant overlap in the return signal, which can lead to ambiguities in detection. For the same pulse repetition rate, using shorter pulses can remedy this problem.....	2
Figure 2: Probing the same object, a longer incident pulse will result in an ambiguous reflected pulse, where the shorter incident pulse will not.....	3
Figure 3: Splitting of 4f energy levels in a Tm^{3+} ion [7]. Note that diagram only represents splitting hierarchy, not relative energies.	7
Figure 4: Laser level diagram for a three-level system. Population inversion must be achieved between upper laser level and ground state.	8
Figure 5: Laser level diagram for a four-level system. Population inversion must be achieved between upper and lower laser levels.....	8
Figure 6: Laser level diagram for a quasi-three-level system. Population inversion can be achieved between upper laser level and the upper manifolds of the ground state.	9
Figure 7: Transitions in $2\mu m$ Tm:YAG laser [14].	10
Figure 8: Diagram of beneficial cross-relaxation in Tm:YAG. 1) There are two ions with overlapping quantum states, one in the pump level, one in the ground level. The pump ion decays to the upper laser level and the ground state ion is excited to the upper laser level. 2) Both ions decay to the lower laser level, emitting two laser photons.	11
Figure 9: Diagram of parasitic upconversion process in Tm:YAG. One ion from upper laser level decays to ground state while one excites to pump level.	13
Figure 10: Upconversion rates in Tm:YAG as predicted by Shaw <i>et al.</i> [16].	13
Figure 11: Photograph of bulk Tm:YAG crystal grown by Czochralski method [23].	14
Figure 12: Absorption spectra for 3% and 6%-doped Tm:YAG crystals.	15
Figure 13: Emission spectrum for 6%-doped Tm:YAG crystal.	16
Figure 14: Transmission spectra over pump and wavelength regions for the input coupler coating on Tm:YAG crystals.....	18
Figure 15: Transmission spectra over pump and wavelength regions for the mid-cavity coating on Tm:YAG crystals.....	19
Figure 16: Transmittance spectra for three plane output coupler mirrors.	20
Figure 17: Focusing optics for pump beam.	21
Figure 18: The beam propagation window in LASCAD.	22
Figure 19: Peak output wavelength versus case temperature for Bright Solutions diode laser. Maintaining 785 nm required selecting different case temperatures as the diode current (or output power) was changed.	24
Figure 20: Output spectra for Bright Solutions diode laser at five case temperatures... ..	25
Figure 21: Output power vs diode current for Bright Solutions pump laser. Data was supplied by manufacturer.	26
Figure 22: Diagram of microchip configuration laser gain crystal. Pump beam is at normal incidence to crystal and is focused inside it. Note that length of crystal (L) is less than diameter of pump mode (d).....	28

LIST OF ILLUSTRATIONS (CONT.)

Figure	Page
Figure 23: Photo of Tm:YAG crystal, 6% doping, 1.5 mm thick, AR coated.	29
Figure 24: Plot of expected power absorption in Tm:YAG gain crystal assuming a 20 W pump beam. Different lines represent different doping percentages.....	30
Figure 25: Two-photon absorption coefficient in YAG. Bandgap = 5.5 eV = 225 nm [28].	31
Figure 26: Cavity modes for 2 mm YAG crystal plotted along with Tm:YAG 2.01 μ m emission peak.	33
Figure 27: Photo of acousto-optic Q-switch used in experiment.	34
Figure 28: Rough diagram of original Tm:YAG crystal heat sink design.	35
Figure 29: Photo of Tm:YAG heat sink, original design. Laser crystal is mounted using thermal compound.....	36
Figure 30: Detailed diagram for updated heat sink design. This version features a thinner mounting surface and a counterbored pump window to fit over pump lens mount.	37
Figure 31: Schematic for actively Q-switched Tm:YAG resonator. 1) 785 nm pump laser, 2) pump fiber, 3) pump beam, 4) collimating lens, 5) focusing lens, 6) side 1 coating, AR @ 785 nm, HR @ 2000 nm, 7) 6% Tm:YAG crystal, 8) side 2 coating, AR @ 2000 nm, HR @ 785 nm, 9) AO Q-switch, 10) HR output coupler mirror, 11) laser output.....	38
Figure 32: Temporal evolution of gain and losses in an example passively Q-switched laser. Shortly after the laser gain exceeds the resonator losses, a short pulse is emitted. Once the absorber starts to be saturated, the power rises rapidly [32].....	40
Figure 33: Absorption spectrum for Cr:ZnSe sample collected with Cary 5000 spectrophotometer. Sample was AR coated for all wavelengths shown.	41
Figure 34: Transmission as a function of incident irradiance for several Cr:ZnSe samples [28].....	42
Figure 35: Intensity of signal beam through the length of a SAQS crystal.....	44
Figure 36: Logarithmic plot of transmittance vs. incident irradiance for a SAQS.....	45
Figure 37: Macroscopic (left) and microscopic (right) photos of thermal damage in Tm:YAG gain crystal.	46
Figure 38: Thermal modeling of Tm:YAG crystal and mount, side view (left) and front view (right), pumped with 40 W of power. Temperature scale is relative to cooling block temperature (15°C).....	47
Figure 39: Output power vs incident pump power for Tm:YAG laser.	48
Figure 40: Slope efficiency of Tm:YAG laser cavity for output coupler mirrors of varying reflectivity.....	49
Figure 41: Threshold pump power vs. output coupler reflectivity for Tm:YAG laser cavity.....	50
Figure 42: Full output spectrum for Tm:YAG laser. Vertical axis is linearly scaled.....	51
Figure 43: Largest peak of output spectrum for Tm:YAG laser. Vertical axis is linearly scaled.	51

LIST OF ILLUSTRATIONS (CONT.)

Figure	Page
Figure 44: Output beam profile for Tm:YAG laser. The upper left and upper right plots show beam waist (in vertical and horizontal dimensions, respectively) as a function of propagation distance, while the bottom plot shows Gaussian fits to the aforementioned beam waist plots.....	52
Figure 45: Example of pulsed output from actively Q-switched Tm:YAG laser. Pulse width is approximately 400 ns.	53
Figure 46: Relative populations of effective inversion, saturable absorber excited state, and number of photons in a laser pulse for a simulated Tm:YAG laser system. Time scale was chosen to emphasize pulse formation.....	59
Figure 47: Relative populations of effective inversion, saturable absorber excited state, and number of photons in a laser pulse for a simulated Tm:YAG laser system. Time scale was chosen to emphasize pulse decay.	60

LIST OF TABLES

Table	Page
Table 1: Relevant energy levels of Tm:YAG [8].	7
Table 2: Experimental values for absorption cross-section of Tm:YAG at 785 nm pump.	12
Table 3: Experimental values for absorption cross-section of Tm:YAG	12
Table 4: Optical and spectroscopic properties for thulium-doped YAG.	16
Table 5: Thermal and mechanical properties for YAG.....	16
Table 6: Pump beam diameter at focus.....	23
Table 7: Data sheet for Bright Solutions pump diode laser and associated optics.	27
Table 8: Summary of published doping levels and gain medium geometries for Tm:YAG lasers.	32
Table 9: Variables for Laser Modeling.....	61

ACKNOWLEDGEMENTS

I would like to thank the Air Force Office of Scientific Research and the Dayton Area Graduate Studies Institute, whose funding efforts made this thesis possible. I would also like to express my sincere gratitude to my thesis committee, my colleagues in the AFRL Electro-Optic Countermeasures group, and my family and friends, without whom none of this would be possible. I would like to offer special thanks to Drs. Ken Schepler, Patrick Berry and Peter Powers for their continued mentorship and professional guidance.

Chapter 1 – INTRODUCTION

1.1 Motivation

Lasers operating in the 2 μm region, especially pulsed lasers, have been proposed for applications in a wide variety of fields. 2 μm radiation is strongly absorbed by liquid water and therefore human tissue, making it useful as a surgical laser. In the lab, 2 μm works as a pump source for non-linear crystals or for other laser systems such as $\text{Cr}^{2+}:\text{ZnSe}$. There is special interest in 2 μm laser sources for military applications: 2 μm is both eye-safe (as compared to $<1.5 \mu\text{m}$ lasers) and shows low atmospheric absorption, making it an excellent wavelength for remote sensing, laser radar, infra-red countermeasures, and optical communications.

Owing to this versatility, there has been strong interest in developing 2 μm sources that are compact, rugged, and capable of operating at or near room temperature. While some progress has been made on quantum well lasers [1], these design constraints typically limit us to solid state lasers using either thulium (Tm), holmium (Ho), or both as the active ions. These rare earth ions can be doped into several crystal host materials such as $\text{Y}_3\text{Al}_5\text{O}_{12}$ (YAG), LiYF_4 (YLF), and YAlO_3 , or into glass hosts such as SiO_2 , making fiber amplification a possibility. These materials, which had previously required flashlamp pumping, may now be pumped with off-the-shelf diode lasers. While thermal management can be a difficulty when running these lasers at very high powers ($>100 \text{ W}$), appropriate cooling can typically be achieved by water/thermoelectric cooling systems. Combined with the naturally-sharp emission peaks of rare earth ions, these characteristics make thulium and holmium excellent choices for a wide variety of field applications.

Many of these applications require that the laser be run in pulsed mode. In laser radar systems, fast beam modulation is correlated with both temporal and spatial resolution. A pulsed beam allows for continuous tracking of an object's movement. Having the shortest possible pulses allows the radar system to operate at higher pulse repetition rates, giving the best possible temporal resolution without dispersion of the reflected pulses introducing ambiguities into the detection scheme (Figure 1).

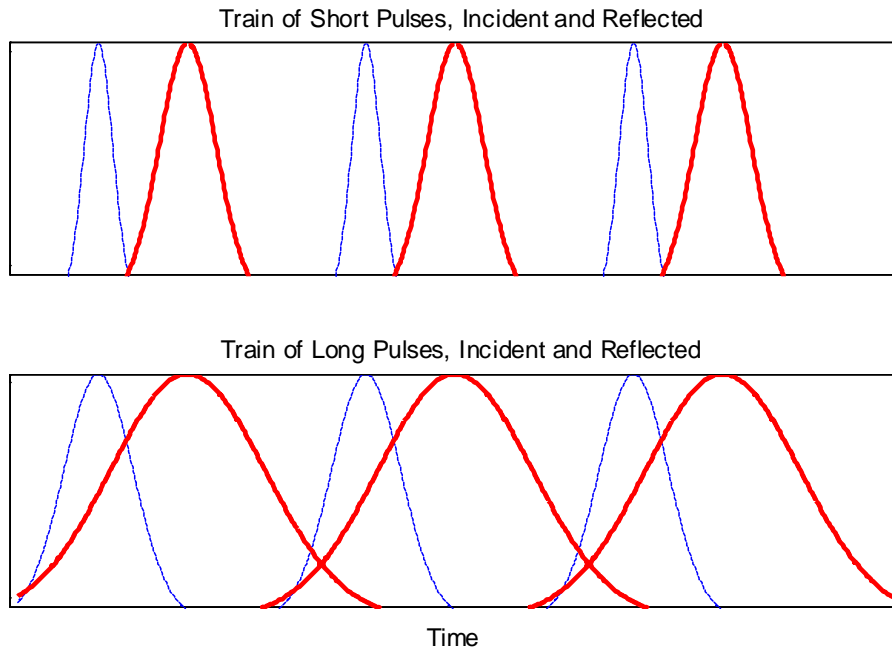


Figure 1: Incident (blue) and reflected (red) signals, with dispersion, for a hypothetical laser radar system. Note that in the case of the longer pulses, there is significant overlap in the return signal, which can lead to ambiguities in detection. For the same pulse repetition rate, using shorter pulses can remedy this problem.

Short pulses are also advantageous in terms of transverse spatial resolution. When one pulse is incident on a surface of varied depth, the ability to resolve the difference in depth is contingent on the pulse being short enough (Figure 2).

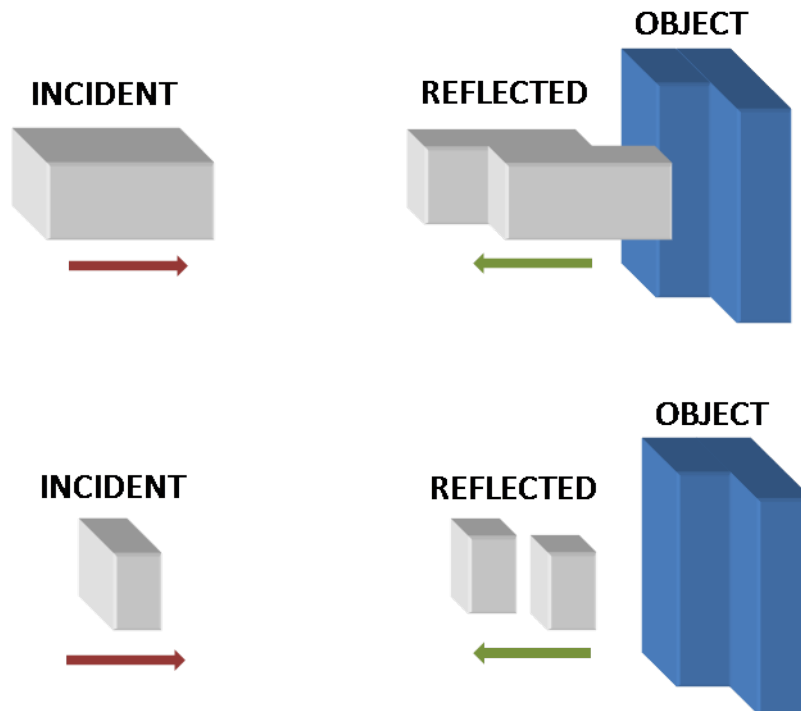


Figure 2: Probing the same object, a longer incident pulse will result in an ambiguous reflected pulse, where the shorter incident pulse will not.

Pulsed laser output may be generated through a variety of methods, but the most common are gain switching, mode-locking, and active and passive Q-switching.

Gain switching, in a solid state laser, is the process of optically-pumping a lasing medium with a source that is itself pulsed [2]. While this is an effective method, it typically does not result in the high-energy pulses common to mode-locking and Q-switching. It also may prove difficult to find pulsed off-the-shelf diode lasers for pumping a solid state medium.

Mode-locking is a set of techniques for synchronizing the phase of all modes oscillating in a cavity at one time, the constructive interference of which yields very short, very energetic pulses [3]. Though mode-locking may demonstrate very effective performance, the implementation can be very difficult and often cost-prohibitive.

In a Q-switched laser, a device is placed within the cavity which is designed to modulate the laser's quality factor, or Q , which in turn determines whether or not the cavity will meet the lasing threshold. An externally-modulated (or *active*) Q-switch may be as simple as a spinning mirror, but they are most commonly built from either an electro-optic crystal (refractive index is changed in the presence of an electric field), or an acousto-optic crystal (acoustically-induced diffraction). Acousto-optic crystals offer a fast method of Q-switching (kHz repetition rate) with good shot-to-shot consistency and the flexibility of external modulation, but they introduce large electrical components into the resonator cavity, therefore lengthening it and increasing the lasing threshold, and require at least some degree of freespace coupling.

Passive Q-switching replaces the electrically-modulated device with an absorbing medium that is easily saturated at the laser wavelength. This saturable absorber introduces a passive loss to the cavity that is inversely proportional to the intensity of

circulating laser radiation. If the saturable absorber parameters are chosen properly, it has a modulating effect on the cavity, oscillating the gain above and below threshold and subsequently creating short, intense pulsed output. Passive Q-switching is generally simple and inexpensive to implement while introducing minimal additional complexity to the laser apparatus. However, individual saturable absorber devices lack versatility, as they must be carefully designed for individual applications and cannot tolerate much variation in operating parameters even within their intended system. The adjustments that *can* be made typically affect other system parameters in potentially undesirable ways; for example, adjusting the modulation rate requires variation of the intracavity irradiance.

To keep these pulses as short as possible while maintaining a simple overall design, a microchip-configuration resonator – a short lasing medium using planar coupling mirrors and a minimal length cavity – is a prudent choice. Given that a circulating pulse generally has to make several round trips through the cavity before it can be fully emitted, shortening the cavity and therefore the round-trip time will shorten the output pulses as well. Additionally, the microchip configuration provides several advantages in terms of output quality. A shorter lasing medium leads to a larger free spectral range such that fewer cavity modes overlap with the gain bandwidth and hence fewer modes can oscillate (see section 3.4), making the laser radiation more spectrally-pure. Furthermore, thermal lensing will generally be less prominent simply because there is less length over which it may affect the beam.

The most obvious disadvantage to this configuration is a shortened gain length, which makes it far more difficult to reach the lasing threshold than in a rod or slab configuration. This must be balanced with a high dopant level, but care must be taken to not concentrate the active ion so densely that undesirable nearest-neighbor effects become prominent. There is also very little volume through which to dissipate waste heat, making thermo-mechanical damage a consideration (especially at high pump irradiance).

Diode-pumped, Tm:YAG microchip lasers have been demonstrated in the literature by Heine and Huber [4] and others, while passive Q-switching of 2 μm lasers by a chromium-doped zinc selenide has been demonstrated by Tsai and Birnbaum [5]. However, combining the two technologies poses a considerable design challenge, as the additional passive losses introduced to the resonator cavity by the saturable absorber crystal must be reconciled with the already significant difficulty of reaching the lasing threshold in a short lasing medium with a small absorption cross-section.

With this laser design, we hope to build on previous work done by our group on pulsed 1.5 μm sources [6]. In that experiment, a pulsed 1 μm seed laser was put through a fiber amplification stage, then converted to 1.5 μm using a non-linear crystal. For the project discussed in this thesis, we concern ourselves with developing a 2 μm laser that can later be used to seed a 2 μm fiber amplifier.

1.2 Overview of Thesis

In this thesis we discuss the design, simulation, construction, and characterization of an actively Q-switched, diode-pumped solid state laser operating at 2 μm .

In Chapter 1 we discuss the motivations behind the development of pulsed 2 μm laser sources and introduce some of the technological challenges that must be surmounted in the design of these lasers.

Chapter 2 is a review of the material and spectroscopic properties of thulium-doped YAG as they relate to laser system design. The origin of the energy level structure for thulium ions is discussed, leading into the properties of the laser transition of interest. We briefly summarize the characteristics of YAG as a laser host material, as well as production techniques, and close with a collection of material data relevant to our experiment.

Chapter 3 reiterates our objectives in the design and construction of a pulsed 2 μm laser system and details the steps taken to meet these objectives for each component of the laser system.

In Chapter 4 a design is presented for replacing our acousto-optic Q-switch with a chromium-doped zinc selenide crystal acting as a saturable absorber passive Q-switch.

Chapter 5 is a summary of the results of our experiments in running our laser system in both pulsed and continuous mode. We attempt a comprehensive characterization of the laser output.

Finally, in Chapter 6 we make closing remarks along with outlining our plans for future improvements to the laser system.

Chapter 2 – MATERIAL CHARACTERIZATION

In the following chapter we review the material and spectroscopic properties of thulium-doped YAG as they relate to laser system design. The origin of the energy level structure for thulium ions is discussed, leading into the properties of the laser transition of interest. We briefly summarize the characteristics of YAG as a laser host material, as well as production techniques, and close with a collection of material data relevant to our experiment.

2.1 *Energy Level Structure*

The thulium atom is a rare earth metal from the lanthanide series having the electron configuration $[\text{Xe}]4f^{13}6s^2$. As with all lanthanides, ionization strips thulium of its 6s electrons to form a trivalent cation, Tm^{3+} . When inserted into a crystal lattice, the thulium ion's outer 5s and 5p shells shield the 4f electrons. The noteworthy consequences are that 1) only the 4f electrons are optically active since 4f is the only partially filled shell, and 2) the effects of ligand interaction on optical transitions are insignificant. These properties give thulium relatively sharp absorption and emission peaks that are largely insensitive to the host material [7].

The following diagram shows the splitting hierarchy for the thulium ion's 4f energy level (Figure 3). The first tier of splitting is the result of interactions between 4f electrons based on their spin and orbital angular momentum quantum numbers (typically denoted as S and L , respectively). The second split is caused by spin-orbit coupling and is determined by the total angular momentum, J . The final and weakest tier comes from interaction between 4f electrons and the lattice structure.

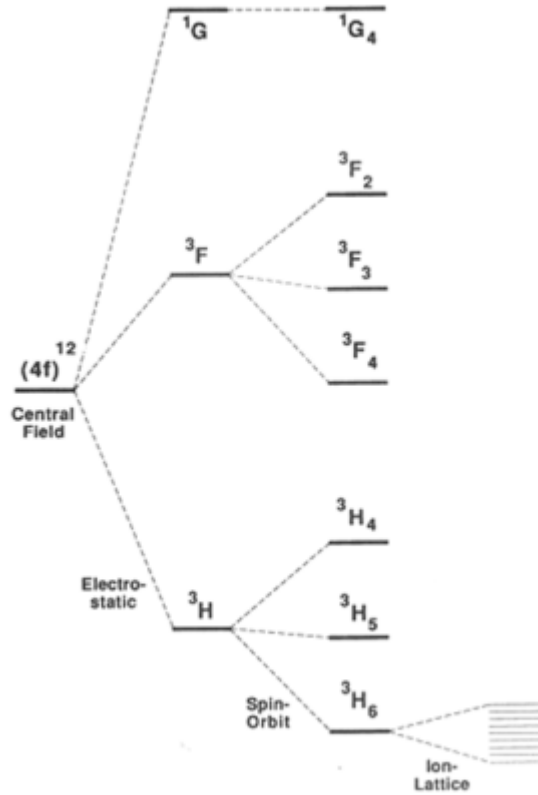


Figure 3: Splitting of 4f energy levels in a Tm^{3+} ion [7]. Note that diagram only represents splitting hierarchy, not relative energies.

Thulium's atomic structure allows it to be used as a dopant for many glass and crystal host materials. For the application discussed in this report, the host crystal is yttrium-aluminum-garnet, or YAG ($\text{Y}_3\text{Al}_5\text{O}_{12}$), where the thulium atom preferentially replaces the chemically-similar yttrium in the crystal lattice. Given that thulium and yttrium both have a charge of +3 in this lattice and have nearly identical ionic radii, the vacancy left by a displaced yttrium ion is an easy match for a thulium ion.

Details of the resulting energy level structure can be found in Tiseanu *et al* [8], while the energy levels relevant to our laser transition are listed in Table 1.

Table 1: Relevant energy levels of Tm:YAG [8].

Energy Level Designation	Centroid (cm^{-1})	Role in Laser System
$^3\text{H}_6$	451	Ground/Lower Laser Manifold
$^3\text{F}_4$	5982	Upper Laser Level
$^3\text{H}_5$	8629	Intermediate State
$^3\text{H}_4$	12889	Pump Level

2.2 Laser Transitions

As the Tm:YAG laser does not strictly obey the dynamics of a true three- or four-level laser system, we must first introduce the concept of the *quasi*-three level system in order to offer a comprehensive description of Tm:YAG transition dynamics.

2.2.1 Quasi-Three Level Systems

While the energy structures of most common laser gain media can be considered as three- or four-level systems without much loss of specificity, there are other media whose most salient characteristics can only be described by assuming the medium behaves as a combination of a true three level and a true four level system. A four-level system comprises a ground state, a pumped state, and upper and lower laser levels (Figure 4). In a three-level system, the ground state and lower laser level are the same (Figure 5). Achieving a population inversion in a three-level system is generally much more difficult than four-level systems because a significant portion of the ground state must be depleted. In a so-called “quasi-three-level” medium, the ground state and lower laser level are both part of the same energy state manifold, but they are far enough apart that it's possible to obtain an inversion between the upper laser level and the lower laser level section of the manifold without necessarily strongly depleting the ground state [9] (Figure 6).

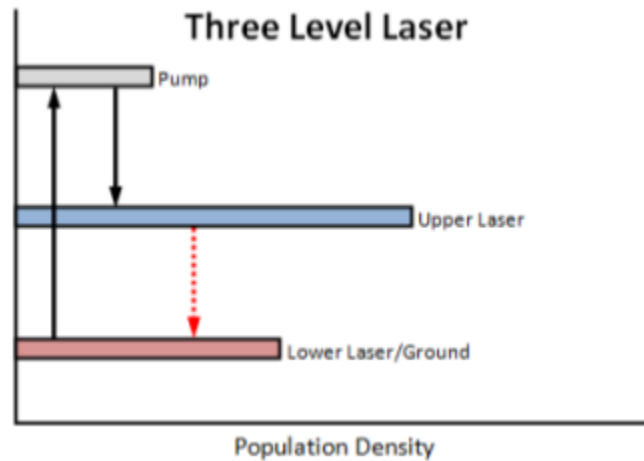


Figure 4: Laser level diagram for a three-level system. Population inversion must be achieved between upper laser level and ground state.

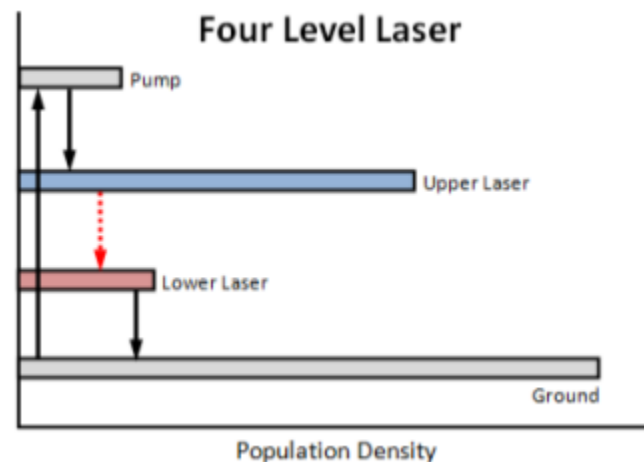


Figure 5: Laser level diagram for a four-level system. Population inversion must be achieved between upper and lower laser levels.

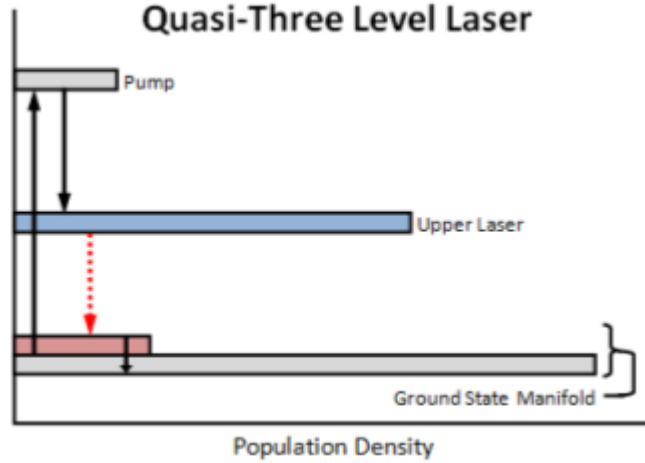


Figure 6: Laser level diagram for a quasi-three-level system. Population inversion can be achieved between upper laser level and the upper manifolds of the ground state.

This is effectively a four-level process, though the distinction from a true four-level system can become very relevant depending on the specific thermal parameters of the material.

The levels of the ground state manifold (GSM) will be populated in accordance with the Boltzmann principle [10]. This principle states that, for any set of atoms in thermal equilibrium, the ratio of population in energy levels E_1 and E_2 may be expressed as:

$$\frac{N_2}{N_1} = \exp \left(-\frac{E_2 - E_1}{kT} \right) \quad (2.1)$$

where k is Boltzmann's constant and T is the equilibrium temperature in Kelvin. As the temperature of the host material is cooled, population drops into the lowest levels of the GSM, creating favorable conditions for obtaining a population inversion with the upper levels and achieving the desired four-level behavior. However, for most quasi-three level gain media, the upper levels of the GSM are thermally-populated at room temperature. This means that population is distributed more uniformly throughout the GSM, leading to transition behavior more akin to that of a true three-level system. In this case, factors other than the size of the population inversion, such as absorption and emission cross-sections, become more prominent in determining which modes will lase. There will also be new losses from reabsorption across the laser transition. Not only is the gain medium more difficult to pump, it may also suffer from stronger mode competition and the instability that accompanies it [11].

2.2.2 Origin of the Laser Transitions in Rare Earth Ions

In free rare earth ions, f-f electric-dipole transitions are forbidden, as all f states share the same even/odd parity; any transition between these states occurs via magnetic-dipoles. In a solid, when the ions are placed into sites which lack inversion symmetry, there is enough mixing of states to turn these forbidden transitions into partially-allowed transitions. While this field distortion introduces only minute perturbations to the ion's energy level structure, the increase in electric-dipole transition rates is enough to produce the transition behavior necessary for laser operation [12].

Particulars of the laser transition of interest in thulium will be detailed in the following section.

2.2.3 Properties of the Laser Transition in Thulium

In the Tm^{3+} ion, the 2 μm laser transition is between the $^3\text{F}_4$ and $^3\text{H}_6$ energy manifolds (Figure 7). The wavelength for the pump laser is typically either 780 or 785 nm, as there are strong absorption lines at both (see section 2.5). This excites the ground state ion into the $^3\text{H}_4$ manifold, where it decays to the $^3\text{H}_5$ manifold via radiative and non-radiative processes, then down to the upper laser level non-radiatively. This transition, which results in a photon with a wavelength of 2.019 μm , has a lifetime of 11 μs and an emission cross-section on the order of $5 \times 10^{-21} \text{ cm}^2$ [13]. Probability of this transition and its emission can either be assisted by cross-relaxation of the pump level, or impeded by the reverse of that process, upconversion. The following section discusses both of these processes, the various secondary transition mechanisms accompanying the stimulated emission, and offers further details of the laser transition itself.

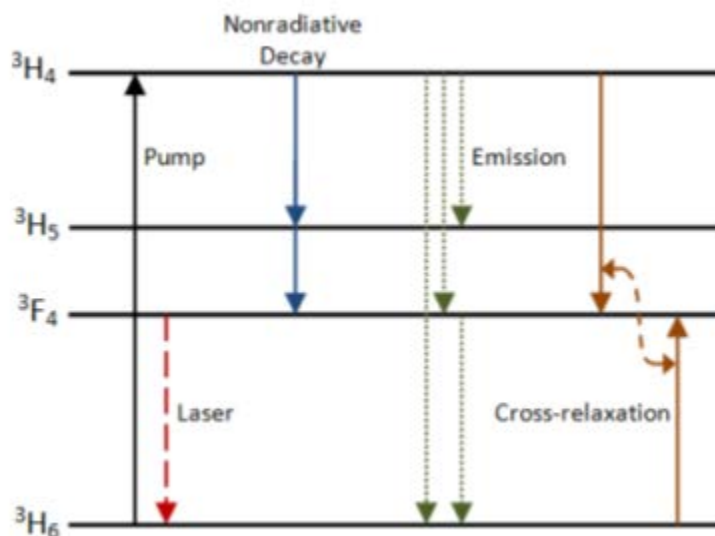


Figure 7: Transitions in 2 μm Tm:YAG laser [14].

Both beneficial and detrimental secondary processes exist in Tm:YAG laser systems and must be balanced by appropriate choice of doping level and pumping scheme [15]. Cross-relaxation of pump ions can give a quantum efficiency that is effectively double that of direct relaxation alone. As an ion in the $^3\text{H}_4$ (pump) level decays to the upper laser level, it may also excite an additional ion from the ground state, through a quantum interaction, to the upper laser level (Figure 8). This effect, the magnitude of which scales with increasing doping level [16], can provide slope efficiency gains reportedly as high as an additional 20% [17]. However, increasing the doping level may give rise to other undesirable effects, such as upconversion and re-absorption losses. Upconversion parasitically depletes the pump level, thereby increasing the pump threshold and adding to thermal losses. As Tm:YAG is a quasi-three level system with a thermally-populated lower laser level at room temperature, re-

absorption of laser radiation by this level may introduce significant loss and contribute to ground state depletion.

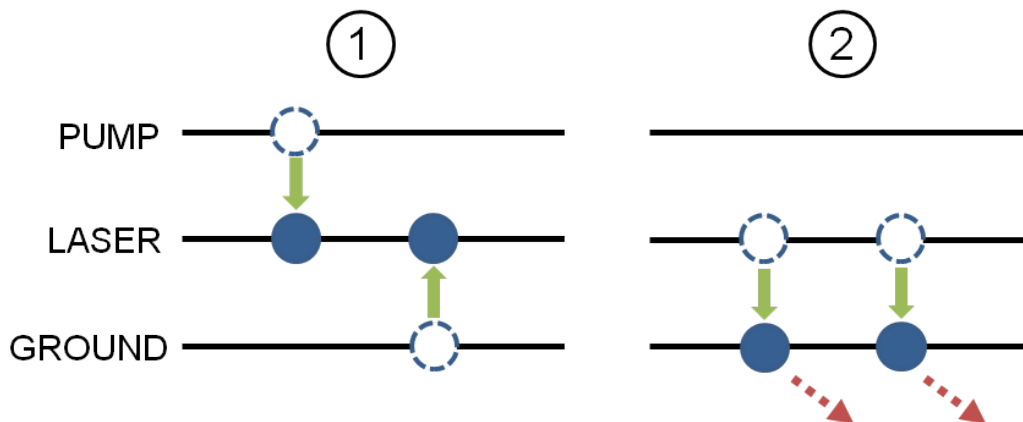


Figure 8: Diagram of beneficial cross-relaxation in Tm:YAG. 1) There are two ions with overlapping quantum states, one in the pump level, one in the ground level. The pump ion decays to the upper laser level and the ground state ion is excited to the upper laser level. 2) Both ions decay to the lower laser level, emitting two laser photons.

The complex interdependences of these processes result in a system of rate equations too intricate to be solved analytically. Optimization of Tm:YAG lasers is best accomplished through rate equation modeling, which we attempt in Appendix A.

In addition to the radiative relaxation processes, the rare earth ions exhibit non-radiative transitions as a consequence of their interactions with the host crystal. This relaxation results in the emission of one or more phonons, or lattice vibrations – typically multiple phonons are emitted, given that the energy differences between Stark levels are often much larger than kT . Since there is large variation in the properties of the lattice for the various rare earth host crystals, the energy of the individual emitted phonons is strongly host-dependent [7]. The rates of non-radiative decay scale with increasing temperature [18], but an exact temperature dependence is difficult to determine [11].

The Tm^{3+} ion is generally recognized to have a low absorption cross section compared to other typical laser ions, thus requiring high pump intensities to meet lasing threshold. In the following table are measured values for the Tm:YAG absorption cross-sections along with our own measured value. Our cross-section was calculated using the absorption spectrum from section 2.5. The details of the calculation can be found in appendix A.3.

Table 2: Experimental values for absorption cross-section of Tm:YAG at 785 nm pump.

Absorption Cross-Section	Reference
$6.5 * 10^{-21} \text{ cm}^2$	[11]
$9 * 10^{-21} \text{ cm}^2$	[17]
$4.8 * 10^{-21} \text{ cm}^2$	[13]
$5.4 * 10^{-21} \text{ cm}^2$	In-house

While we were not able to measure the stimulated emission cross-section directly as we did not have a blackbody-calibrated monochromator at the time, we were able to obtain several values for the 2.02 μm peak's emission from the literature which can be seen in the following table.

Table 3: Experimental values for absorption cross-section of Tm:YAG

Stimulated Emission Cross-Section	Reference
$5 * 10^{-21} \text{ cm}^2$	[11]
$5 * 10^{-21} \text{ cm}^2$	[15]
$2 * 10^{-21} \text{ cm}^2$	[19]

While the potential for tunability in rare earth lasers is generally thought to be limited owing to weak vibronic coupling of optically-active electrons, Tm^{3+} has the advantage of a high number of closely-spaced Stark levels and slightly stronger lattice coupling than more common rare earth lasers such as neodymium. Indeed, Stoneman and Estereowitz have demonstrated continuous tuning over the range of 1.85 to 2.16 μm for a Tm:YAG laser [17]. Even broader tuning is possible in glass hosts [7]. For the purposes of this thesis, we will restrict ourselves to investigation of single-frequency operation at 2.02 μm .

As mentioned previously, there is an additional undesirable energy transfer mechanism in Tm:YAG called upconversion, which diminishes the laser's quantum efficiency and consequently raises the pump threshold. In upconversion transitions, there is a quantum interaction between two Tm^{3+} ions in the upper laser level ($^3\text{F}_4$) resulting in one ion exciting into either the $^3\text{H}_4$ or $^3\text{H}_5$ states and one decaying back to the ground state ($^3\text{H}_6$) (Figure 9). This process has a parasitic effect on the pump energy, as (in the general case) only one laser photon is potentially generated for two pump photons.

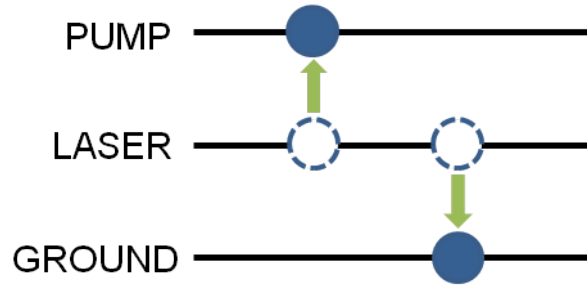


Figure 9: Diagram of parasitic upconversion process in Tm:YAG. One ion from upper laser level decays to ground state while one excites to pump level.

The magnitude of this effect depends on the statistical distance from one active ion to its nearest neighbor [20]. In practice, this means that upconversion becomes more prominent with increasing doping. Shaw et al. have predicted the upconversion rates in Tm:YAG will initially scale exponentially with increasing doping, then level off (Figure 10).

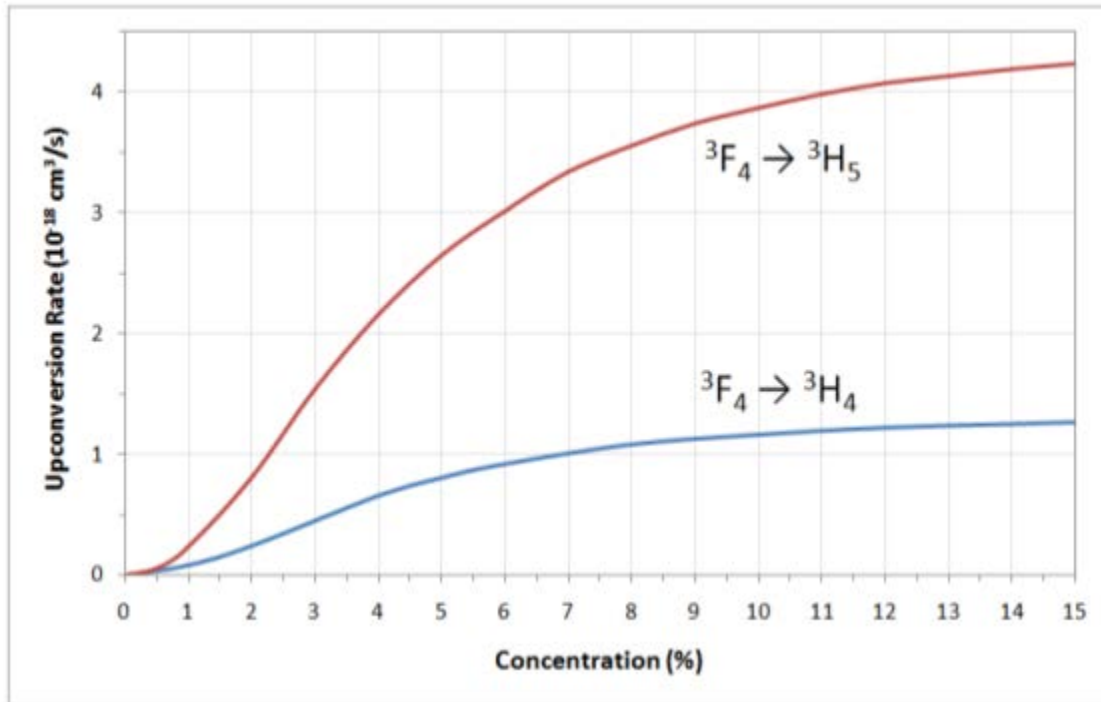


Figure 10: Upconversion rates in Tm:YAG as predicted by Shaw *et al.* [16].

This dependence must be taken into consideration when choosing a doping percentage for a Tm:YAG gain medium: for maximum gain per unit length, the concentration should be as high as possible without upconversion-related self-quenching becoming too prevalent. We will discuss this balance further in section 3.4.

In the general case, Tm:YAG lasers will produce one laser photon per every one pump photon absorbed by an active ion. However, as we have discussed previously, by taking advantage of Tm³⁺'s cross-relaxation properties, a quantum efficiency approaching 2:1 may be achieved. If we assume the effects of excited state absorption

are minimized, our per-photon energy efficiency is between $1 \cdot (780 \text{ nm} / 2020 \text{ nm}) = 37\%$ and $1 \cdot (780 \text{ nm} / 2020 \text{ nm}) = 77\%$.

2.3 YAG

In addition to the aforementioned favorable crystal field characteristics of YAG, it has several thermal, optical and mechanical properties that make it particularly desirable as a laser host material [21]. YAG is structurally strong, optically isotropic, and can be grown to high optical quality. It has no absorption features near the pump or the emission wavelengths for Tm^{3+} . Because of its relatively high thermal conductivity (0.14 W/cm K at 300 K), YAG is capable of handling large pump powers. YAG also has a fairly small thermo-optic coefficient ($7.3 \cdot 10^{-6} \text{ K}^{-1}$), which means the effects of thermal lensing will be less significant than other host crystals such as YAlO_3 ($> 8 \cdot 10^{-6} \text{ K}^{-1}$) or YLF ($< 4 \cdot 10^{-6} \text{ K}^{-1}$) [22]. Finally, as a consequence of its versatility as a host material, it's widely available commercially, typically without requiring a custom growth run.

2.4 Production

$\text{Tm}:\text{YAG}$ is conventionally produced by the Czochralski method, which involves both the host and dopant materials being ground into powders and mixed together, melted into a polycrystalline material, seeded with a crystal of the desired composition, then pulled into a large crystal boule and allowed to cool. The Czochralski method allows for crystals to be grown which are free from or low in impurities, cracking, and non-uniformities in the lattice structure [23]. Atomic doping concentrations of thulium in YAG are typically on the order of 0.1-10%.



Figure 11: Photograph of bulk $\text{Tm}:\text{YAG}$ crystal grown by Czochralski method [23].

2.5 Material Data

2.5.1 Absorption Spectrum

The following Tm:YAG absorption spectra were collected with a Cary 5000 spectrophotometer. 1 mm thick, uncoated spectroscopic Tm:YAG samples at 3 and 6% doping were used. Samples were measured at normal incidence. Fresnel reflection losses, which were not accounted for in the following figure, are calculated to be ~8.5% per side at the pump wavelength (see appendix B.3).

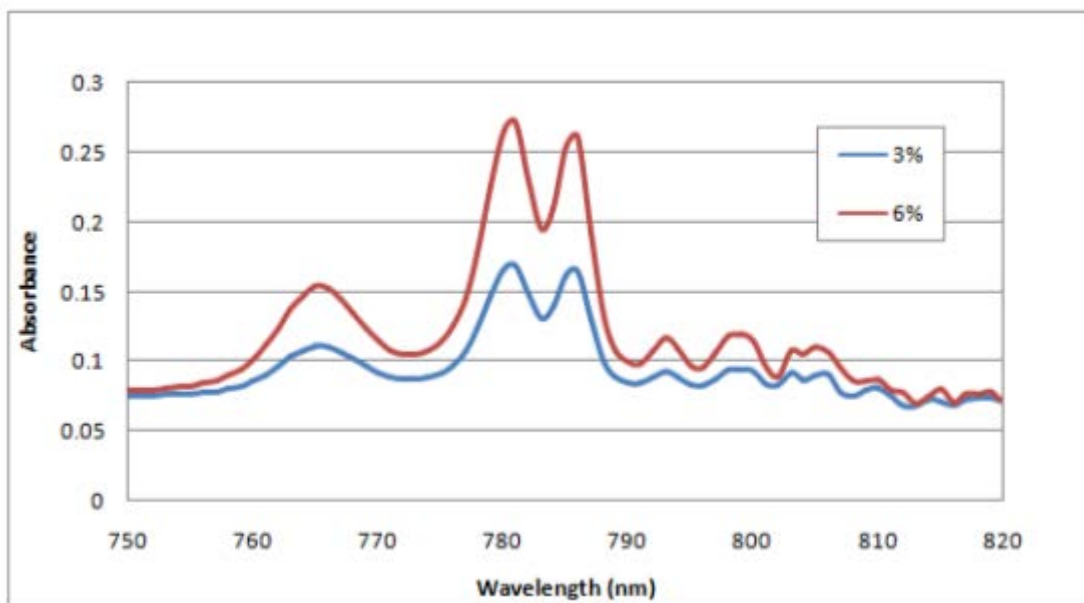


Figure 12: Absorption spectra for 3% and 6%-doped Tm:YAG crystals.

2.5.2 Emission Spectrum

The following plot is an emission spectrum for Tm:YAG. The sample used was an uncoated, 6% doped, 1 mm thick wafer. It was edge-pumped with a 780 nm diode laser running at approximately 1 W. The spectrum was collected with an Acton Research SpectraPro 750 monochromator. The integration time was set to 1200 ms, the resolution was 1 nm, and both the entrance and exit slits were opened to 10 μm . The sample was kept at room temperature.

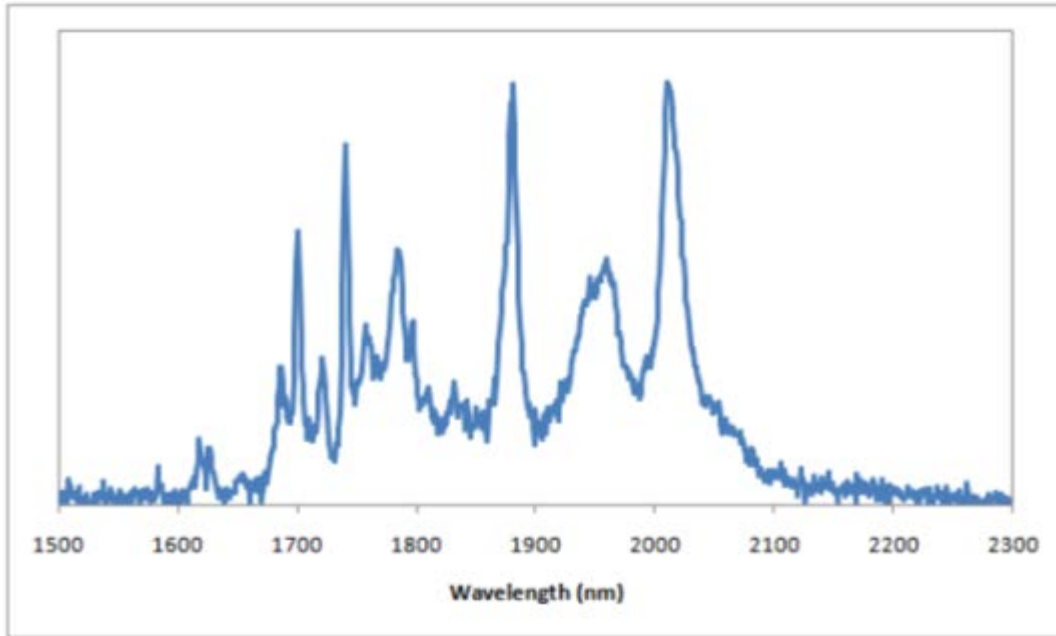


Figure 13: Emission spectrum for 6%-doped Tm:YAG crystal.

2.5.3 Optical and Spectroscopic Properties

Table 4: Optical and spectroscopic properties for thulium-doped YAG.

Description	Value	Reference
Upper state lifetime	12 ms	[11]
Emission cross-section	$0.5 \cdot 10^{-20} \text{ cm}^2$	[11]
Pump absorption cross-section	$0.54 \cdot 10^{-20} \text{ cm}^2$	In-house
Upper level Boltzmann factor	0.46	[11]
Lower level Boltzmann factor	0.017	[11]
YAG refractive index	1.82	[11]

2.5.4 Thermal and Mechanical Properties

Table 5: Thermal and mechanical properties for YAG.

Description	Value	Reference
YAG thermal conductivity	10-14 W/mK	[24]
YAG dn/dt	$7 \cdot 10^{-6} / \text{K}$	[24]
YAG thermal shock parameter	790 W/m	[24]
YAG melting point	2240 K	[24]

Chapter 3 – LASER SYSTEM DESIGN

In this chapter, we reiterate our design objectives and detail the steps taken to meet them for each component of the laser system.

3.1 Overview of Design Objectives

3.1.1 Pulse Width Optimization

As discussed in the introduction, one of our primary design objectives is that the laser have the shortest pulses possible. To address this concern, there are two design parameters (aside from the choice of Q-switch) with which we must concern ourselves: the length of the resonator cavity, which determines the round-trip time of circulating laser radiation, and the reflectivity of the output coupler mirror, which determines how much of a laser pulse is dumped with each round trip and therefore how many round trips must be made to form a complete output pulse.

The round trip time, which is defined simply as the optical path length through the cavity divided by the speed of light, may be minimized by building the cavity as compactly as possible. This is the principal motivation for the choice of a microchip (also called “thin disk”) gain medium geometry. Additionally, with planar resonator mirrors we can push the optical elements as close together as possible, further shortening the round trip time with the added benefit of raising the cavity Q-factor and making it easier to meet the lasing threshold.

Also necessary for shortening pulses is getting the output coupler reflectivity as low as possible while still being able to meet the cavity’s lasing threshold. When a Q-switching device “opens” and a laser pulse is formed, the fraction of the circulating pulse that exits the cavity with each round trip depends on the reflectivity of the output coupler mirror. This determines how many round trips a pulse needs to fully exit the cavity, and consequently, the overall duration of the output pulse. It should be noted that while the lowest possible reflectivity is our eventual goal, we had to start with a high reflectivity mirror to give us the best chance of initially achieving cw laser operation. Most of the experiments detailed in this report used the high-reflectivity mirror.

3.1.2 Spectral Purity

It is well established that good spectral purity results in better performance in laser radar systems [25]. A large linewidth can also translate to added phase noise, which degrades dynamic range and sensitivity of detection [26]. While there are a multitude of techniques for improving spectral characteristics in laser systems, for our simple system we will rely on two particular design choices: a short gain medium to limit the number of modes that will lase, and the use of a rare earth metal as the active ion, which is shielded from lattice broadening by an optically-inactive electron orbital. Further discussions of the theory underlying these two design elements can be found in sections 3.4 and 2.1, respectively.

3.1.3 Other Considerations

There are a number of secondary design objectives which are not critical to proof of concept but, if met, would be advantageous for eventual field applications. For example, nearly any real-world laser system can benefit from robustness of its

components, a compact form factor, and low complexity overall. This is especially true of aircraft and other military vehicle applications, where space comes at a premium and environmental conditions can be severe. To this end, we have chosen to use all solid-state components with minimal lengths of freespace coupling. We have also made efforts to combine components where feasible, such as using dielectric coatings on the gain medium as end mirrors. For thermal management, only fully enclosed water cooling was used and was run at near room temperature.

3.2 Mirrors

3.2.1 Input Coupler Mirror

For the sake of simplicity and compactness, the input coupler mirror was applied directly to the lasing medium as a dielectric coating. The coating, which was contracted out to Blue Ridge Optics, was designed to be highly transmissive at the pump wavelength (to allow pump energy to enter the cavity) and highly reflective at the laser wavelength (to serve as the first resonator mirror). A plot of the coating's transmission, supplied by the manufacturer, may be seen in Figure 14:

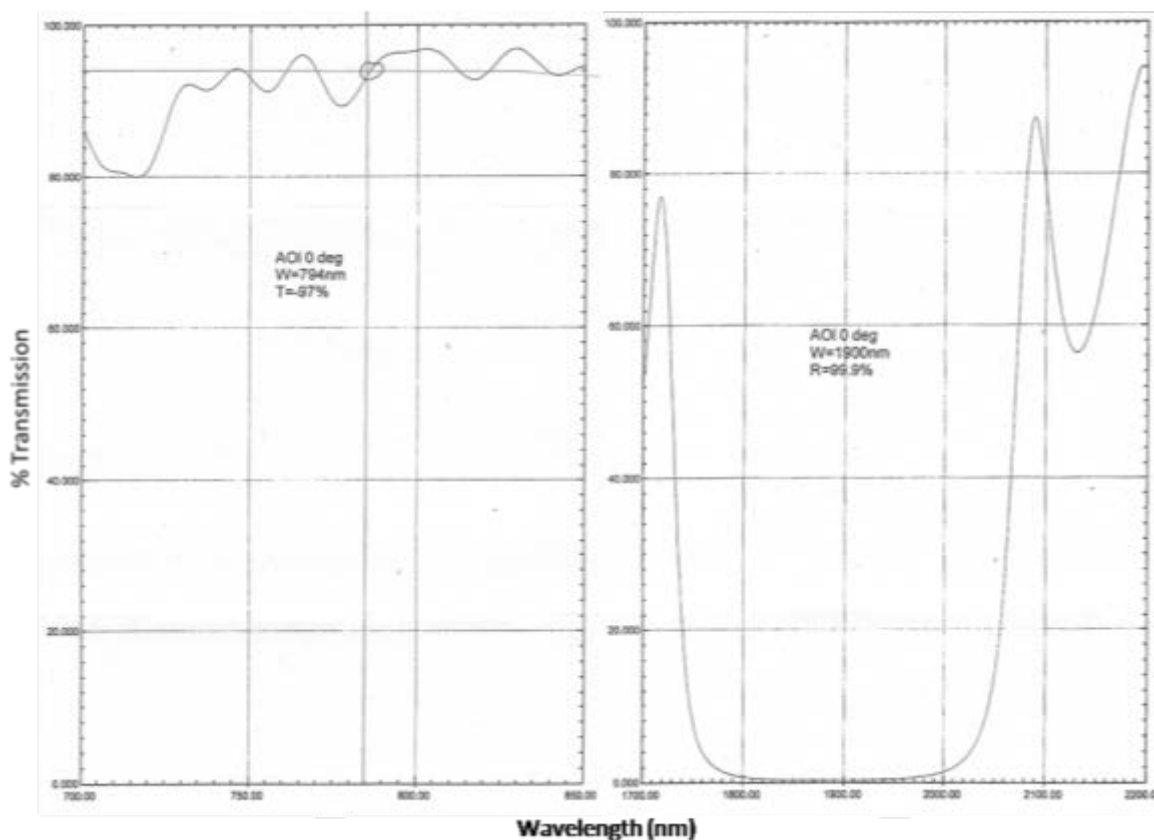


Figure 14: Transmission spectra over pump and wavelength regions for the input coupler coating on Tm:YAG crystals.

3.2.2 Transmissive Coating

The opposite side of the Tm:YAG crystal was also given a dielectric coating to optimize laser performance. This coating is highly transmissive at the laser wavelength, allowing laser light to travel the full length of the cavity unimpeded. It is also highly-

reflective at the pump wavelength, which gives the pump light a second pass through the lasing medium for maximum pump absorption, making it easier to reach the lasing threshold. A plot of this coating's transmission may be seen in Figure 15.

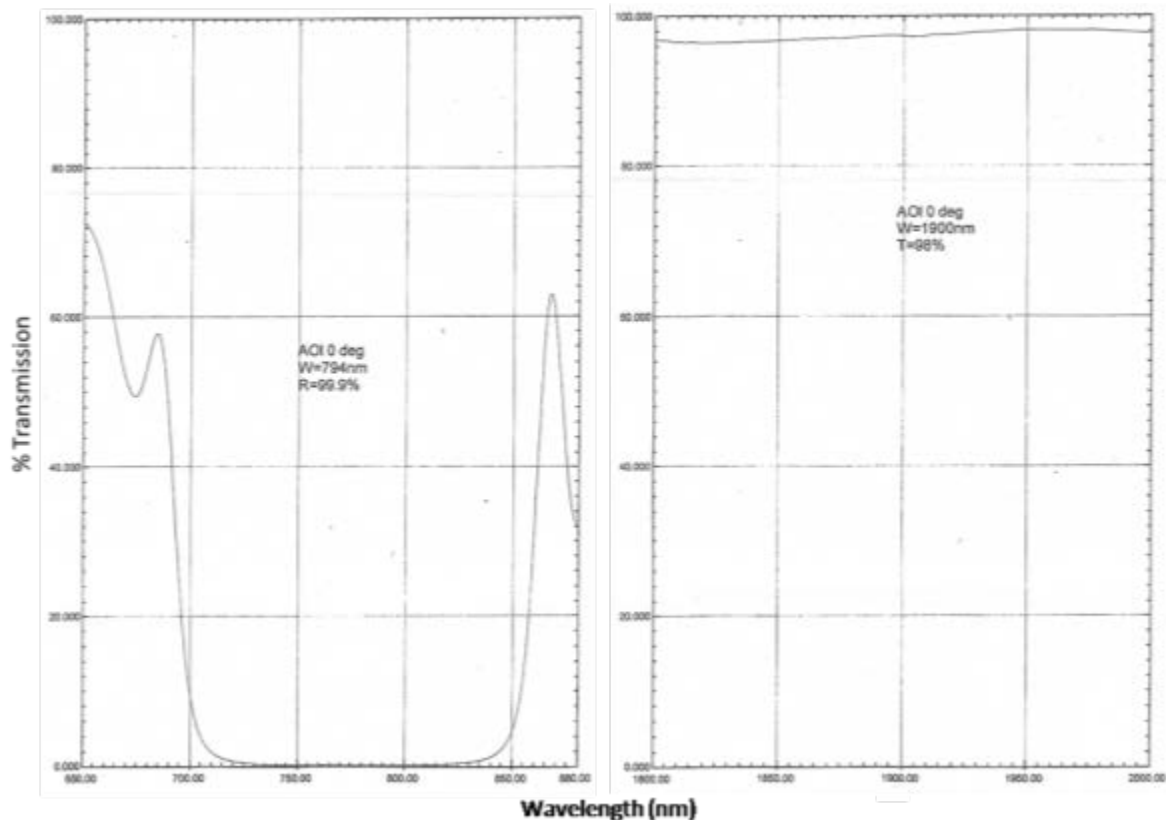


Figure 15: Transmission spectra over pump and wavelength regions for the mid-cavity coating on Tm:YAG crystals.

3.2.3 Output Coupler

Rather than attempt to define the parameters of an optimum output coupler mirror in the design stage, we chose to test mirrors from our existing supplies and verify experimentally which was best-suited to our application. Mirrors with high reflectances were chosen to start to keep the cavity's quality factor high, making it easier to reach lasing threshold. While a focusing mirror might be preferable for cavity stability, we did not have any curved mirrors with focal lengths short enough that it would make a difference to such a short cavity – any of our existing mirrors would have essentially been seen as planar.

Three mirrors with manufacturer-quoted >95% reflectivity were tested in a Cary 5000 spectrophotometer to ascertain their exact reflectivities at our wavelength of interest. In the following figure (Figure 16) is a plot of their measured transmittances:

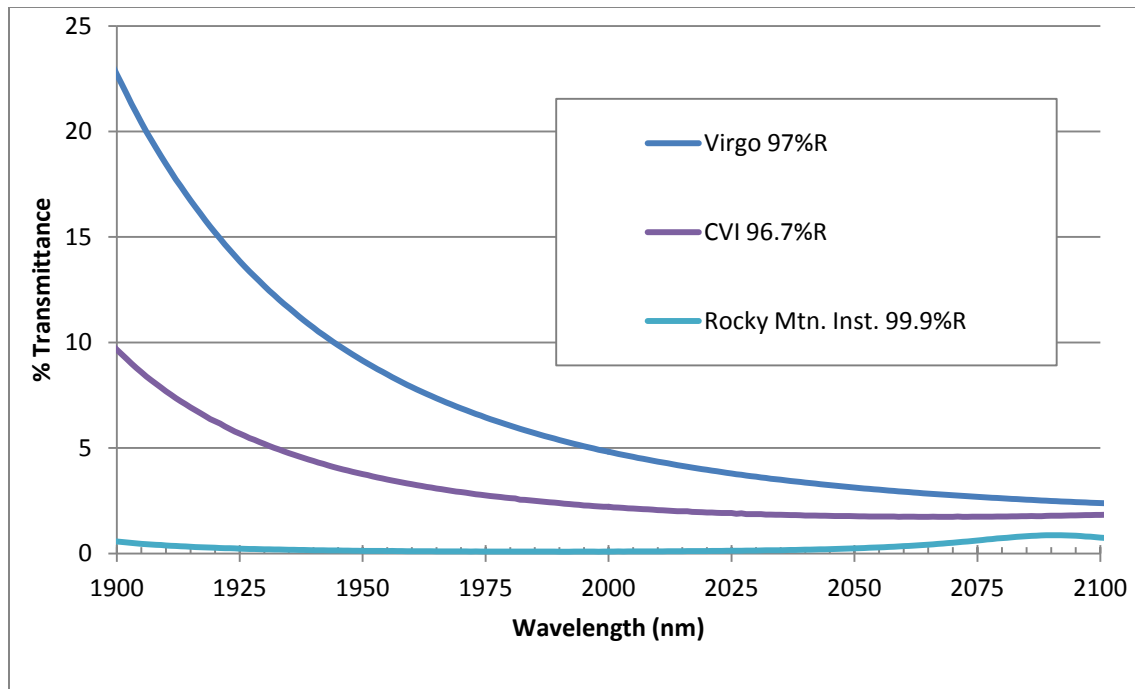


Figure 16: Transmittance spectra for three plane output coupler mirrors.

From this data we see that our chosen mirrors have reflectivities of 96, 98, and 99.9% at the wavelength of interest, 2.01 μm . While mirrors with relatively high reflectivities will help to ensure that the cavity reaches laser operation, it should be noted that this is not the best choice for achieving our primary design objective of generating very short pulses. To this end, the output coupler reflectivity should be minimized so that a circulating pulse may exit the cavity in the fewest passes possible.

For the first iteration of this laser system, it was necessary to use an independent output coupler mirror to be able to both run the laser in CW mode and to accommodate an active Q-switch. However, in the future versions in which we intend to Q-switch the cavity with a saturable absorber crystal, the output coupler mirror will likely be a dielectric coating applied to the saturable absorber crystal face (similar to our current input coupler).

3.3 Pump Sources

3.3.1 Overview

In keeping with the objective of using components robust and portable enough to be integrated into other systems with minimal additional equipment requirements, we have chosen to use a prepackaged, solid state, fiber-coupled diode laser as the Tm:YAG pump source. Given the small absorption cross-section of the gain medium (see section 2.5), a very high output power (relative to the form factor) was required of the pump laser to meet the threshold intensity for the cavity. The pump laser was a custom model purchased from Bright Solutions specified for 30 W of cw power with a center wavelength of 784 nm and a linewidth of <2 nm. The unit was constructed as an array of diode bars all focused into one fiber pigtail.

The transport fiber itself was 3 m long with a 200 μm core diameter. We chose the smallest core diameter fiber available for this laser so that the fiber tip could be imaged to the smallest possible spot in the gain crystal, yielding the highest intensity. Typical of a high-power fiber laser, the fiber is strongly multimode and the laser output is randomly polarized.

Also purchased (though not used in final experimental designs) was a similar diode laser from nLight. This laser offered more available power (40 W), but a larger core diameter fiber (400 μm) meant that the beam would not be able to be focused as tightly. Note: when we mention “the pump laser” in the singular elsewhere in this document, we refer to the Bright Solutions diode laser unless otherwise specified.

3.3.2 Pump Optics

To achieve the highest pump intensity in the gain crystal possible, very short focal length aspheric lenses were used. The system comprised two lenses: a collimating lens that was approximately numerical aperture-matched to the pump fiber output, and a focusing lens (Figure 17). This system effectively allows us to image the tip of the fiber inside the gain crystal; the magnification of the image is proportional to the ratio of focal lengths of the two lenses. Aspheric lenses were used to avoid spherical aberrations, which become more prominent with shorter focal lengths.

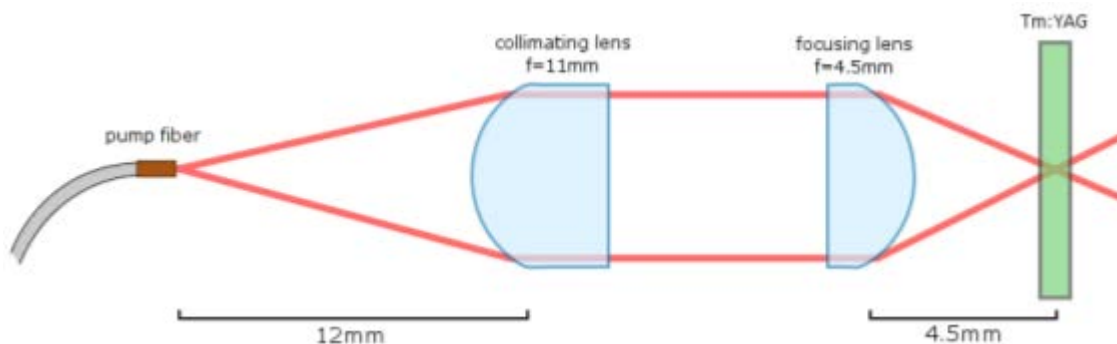


Figure 17: Focusing optics for pump beam.

Placement of optics was first approximated using modeling software (as discussed in the next section), then fine-tuned experimentally. Before introducing the focusing lens, the collimating lens was placed in the beam path and the pump spot was imaged on a screen (viewed with an IR viewer). The lens was translated longitudinally until the image on the screen maintained roughly the same diameter as the screen itself was translated longitudinally. At this point the beam was considered to be collimated and the focusing lens was added.

In the initial design for this experiment, the pump optics used were given Thor Labs' standard visible light anti-reflective coatings. However, these coatings proved to be insufficient for dealing with the high irradiance (up to 500 W/cm^2) of the pump beam when several sustained optical damage during the course of the experiment. The second round of pump optics was given special high-intensity AR coatings by Onyx Optics Inc.

3.3.3 Modeling of the Pump Mode

Prior to construction of the experiment, the pump mode was modeled in LASCAD, a Gaussian beam propagation program. By inputting several starting conditions for a beam such as mode diameter, divergence angle and beam quality, LASCAD will calculate parameters of the beam as it passes through optical surfaces (Figure 18). Using this information, we were able to choose the pump optics best suited to our system.

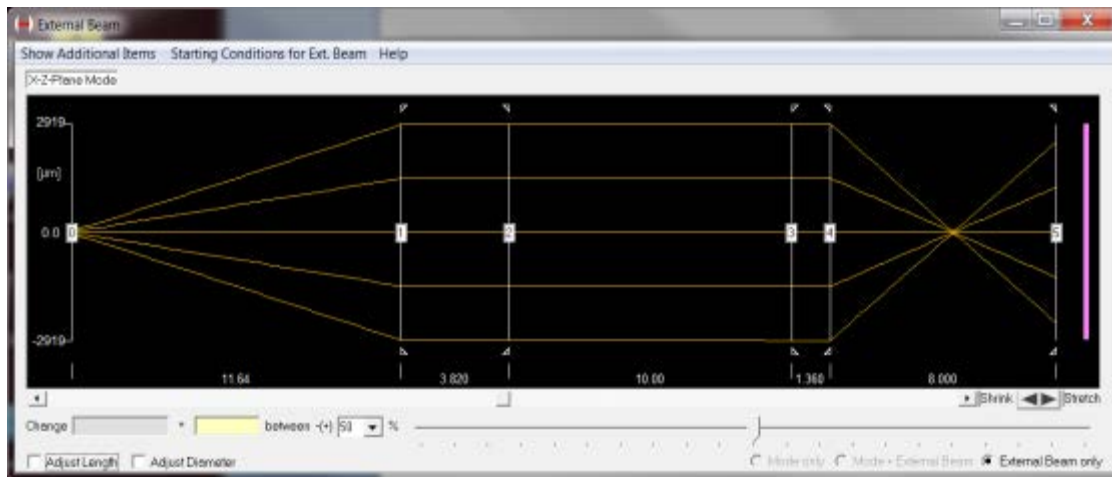


Figure 18: The beam propagation window in LASCAD.

The starting mode diameter was assumed to be the diameter of the fiber core, 200 μm . Divergence angle was calculated from the fiber's numerical aperture (0.22). The beam quality (M^2) was 88 (see appendix A.2). Using these values, the model predicts that the pump mode diameter at the focus will be approximately 100 μm . If the 2 mm-thick Tm:YAG crystal is placed at the focus, the pump mode diameter will be around 700 μm at the faces of the crystal.

3.3.4 Spot Size Measurement

A set of pinhole apertures was used to measure the diameter of the pump beam at its focus. The pump beam was set to a low output power, which was measured directly with a power meter. Then a pinhole of known diameter was mounted to a three-axis stage and placed between the pump laser output and the power meter. The pinhole translation was adjusted in all three directions until the reading on the power meter was maximized. The maximum power passing through the aperture was recorded and the experiment was repeated for a different size pinhole.

We know from manufacturer data that outputs of our pump sources are highly multimode and are therefore not perfect Gaussian beams. We will assume, however, that the shape of the beams may be at least approximated by a perfect Gaussian ($M^2=1$). For a perfect Gaussian beam of diameter w , the power P passing through an aperture of radius r at distance z from the beam waist is:

$$P(r, z) = P_0 \left(1 - \text{Exp} \left[\frac{-r^2}{w^2(z)} \right] \right) \quad (3.1)$$

The results of this measurement and calculation for the nLight pump laser (running at 785 nm) and the Bright Solutions pump laser (running at 780 nm) are shown in the following table:

Table 6: Pump beam diameter at focus

Laser	Radius of aperture (μm)	Gaussian diameter (μm)
nLight Pearl	128.0	157.6
	54.7	141.1
Bright Solutions	128.0	108.3
	54.7	91.6

From these results we may conclude that the diameter of the beam at the waist is between roughly 141 and 158 μm for the nLight and between 91 and 109 μm for the Bright Solutions, which are in good agreement with the values predicted by our simulations discussed in the previous section.

3.3.5 Temperature Control

Temperature control was achieved by mounting the laser to a water-cooled block connected to a thermoelectric chiller. Experimentally, the laser's temperature characteristics were determined by measuring the beam with a spectrometer while varying the chiller temperature. The temperature itself was measured on both the chiller's readout and by the laser diode's internal thermistor. The optimum temperature for pumping the gain medium was confirmed by focusing the pump laser onto the gain crystal and measuring the crystal's fluorescence (with no laser feedback in place) while varying the chiller temperature. When the fluorescence at the desired laser wavelength was maximized, we took that to be our operating temperature.

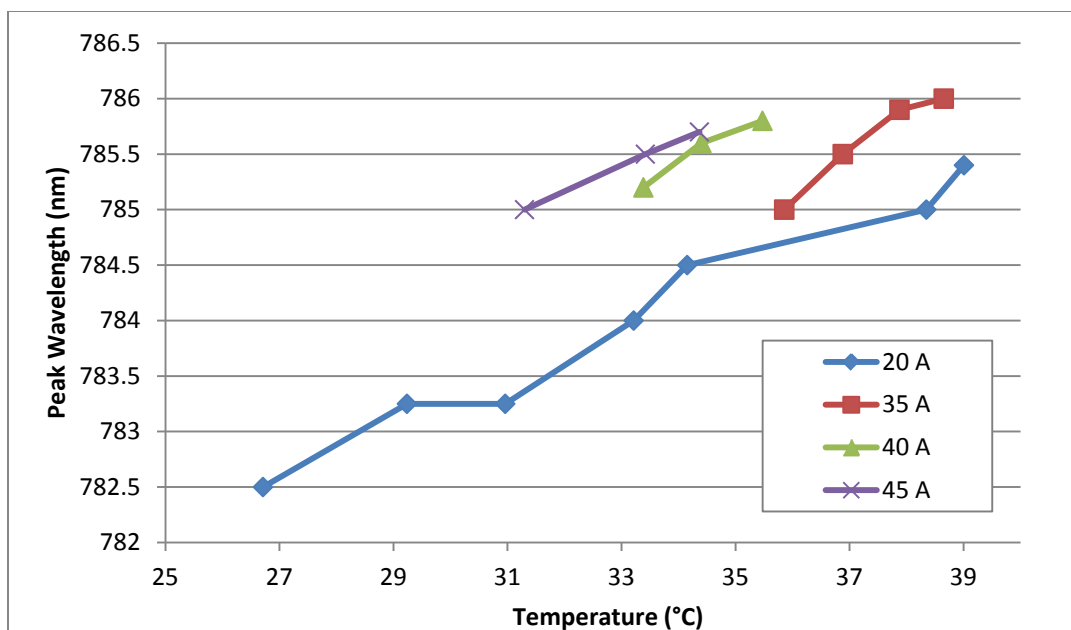


Figure 19: Peak output wavelength versus case temperature for Bright Solutions diode laser. Maintaining 785 nm required selecting different case temperatures as the diode current (or output power) was changed.

While the optimum operating wavelength was chosen by temperature tuning to maximize the crystal fluorescence, the pump laser's output spectrum was still measured at different temperatures to gain a fuller understanding of the laser's output characteristics – specifically, to find the linewidth for the pump peak and observe any variations of the peak shape with changing temperature. The results are in the following plot (Figure 20).

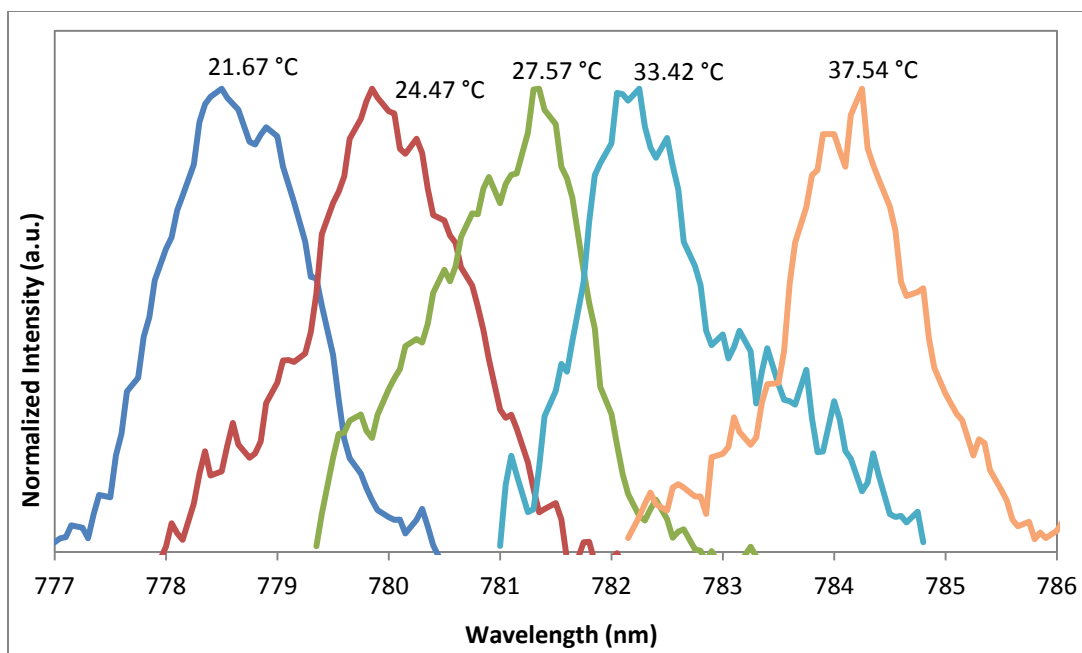


Figure 20: Output spectra for Bright Solutions diode laser at five case temperatures.

These spectra were collected on a Spex 220 spectrometer at the diffraction grating second order (1554 – 1572 nm) then converted to first order. Slit widths were set to 0.1 mm. Laser output power was held at roughly 1 W.

3.3.6 Output Power

The pump laser's output power as a function of applied electrical current may be seen in Figure 21. Varying the current supplied to the diode does produce some changes in the diode's internal temperature even when the system is given sufficient time to reach thermal equilibrium. This is possibly due to non-uniform heating throughout the diode enclosure. Regardless, the chiller was adjusted to maintain our desired temperature at the most useful operating currents.

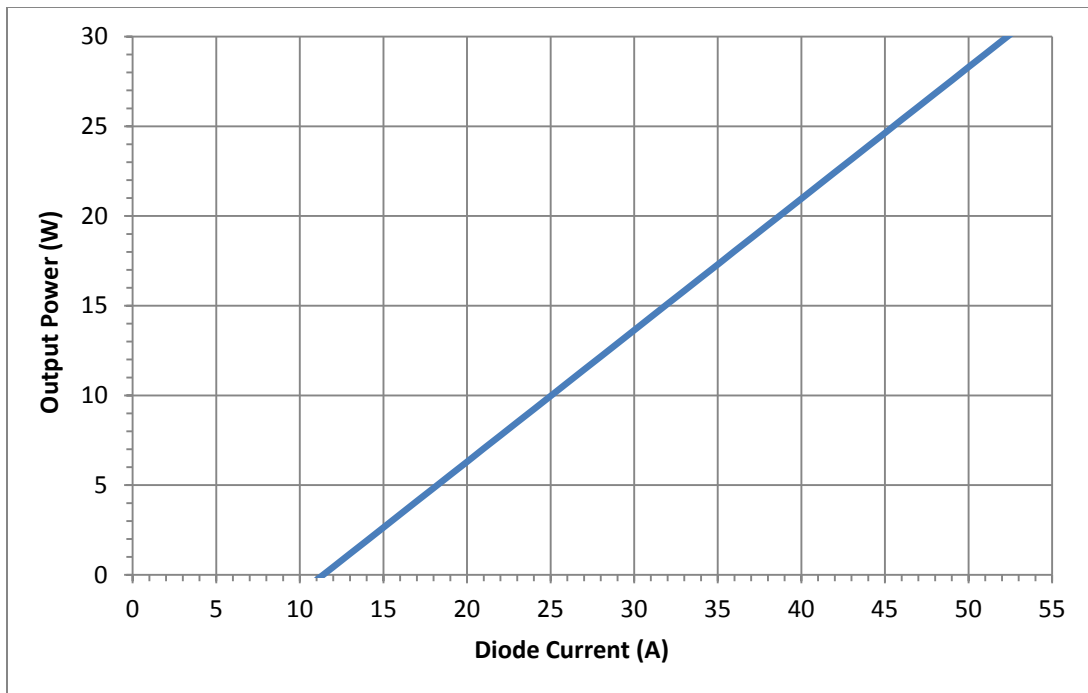


Figure 21: Output power vs diode current for Bright Solutions pump laser. Data was supplied by manufacturer.

3.3.7 Pump Diode Data Sheet

Table 7: Data sheet for Bright Solutions pump diode laser and associated optics.

Optical/Electrical Properties	
Center Wavelength	784.0 nm
Operating Wavelengths	785 nm
Linewidth FWHM	2.0 nm
Beam Quality (M^2)	~88
Beam Diameter at Focus	$90 < \phi < 180 \mu\text{m}$
Max Output Power	30 W
Control Current at Max Power	52 A
Threshold Current	12.5 A
Diode Voltage	1.7-1.9 V
Thermal Properties	
Case Temperature @ 785 nm, 20 W	39°C
Temperature-Wavelength Coefficient	0.23 nm/°C
Fiber Specifications	
Length	3 m
Core Diameter	200 μm
Numerical Aperture	0.22
Pump Optics	
Focal Length, Collimating Lens	11 mm
Lens Diameter, Collimating Lens	7.2 mm
Focal Length, Focusing Lens	4.51 mm
Lens Diameter, Focusing Lens	6.33 mm

3.4 Lasing Medium

3.4.1 Overview

Ideally, a microchip (or thin disk) configuration laser resonator is defined as having a gain medium whose length is less than the diameter of the laser mode as it passes through the gain medium [27]. In practice, this typically means a very thin, wafer-like laser crystal placed in a cavity such that the pump beam is normally incident on the crystal face (Figure 22). As was discussed briefly in the introduction, this system configuration has several advantages in terms of laser performance, particularly for pulsed lasers – namely, good spectral purity and short round trip times.

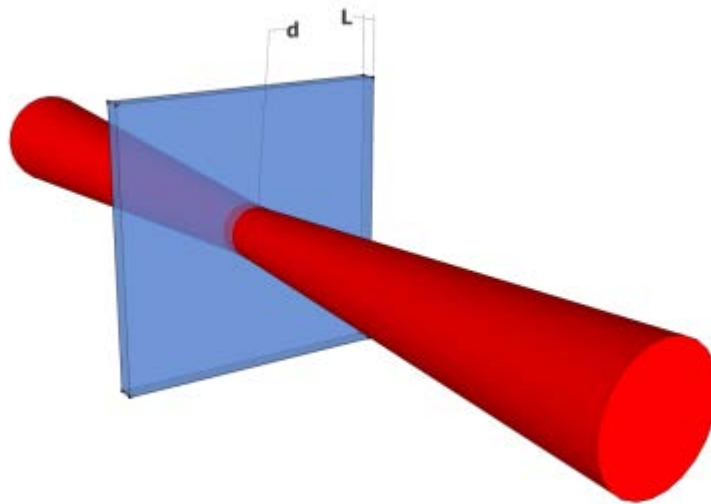


Figure 22: Diagram of microchip configuration laser gain crystal. Pump beam is at normal incidence to crystal and is focused inside it. Note that length of crystal (L) is less than diameter of pump mode (d).

For this experiment, we purchased (from Onyx Optics) two sets of Tm:YAG crystals to test in our laser system: in the first order, a 0.1 and a 0.25 mm thick wafer, and in the second, a 1, 1.5 and 2 mm thick wafer. All crystals were purchased in both 3 and 6% doping concentrations, the latter being the highest we were able to find from any vendor without requiring a custom growth run. All wafers were approximately 5-10 mm square and were given AR/HR coatings, the details of which are discussed in section 3.2. In addition to the laser crystals, 3 and 6% uncoated samples were purchased for use in spectroscopic characterization experiments. Note that for the experiments discussed in this thesis, the 2 mm, 6%-doped Tm:YAG sample was used unless otherwise noted.

In the following sections, we discuss the calculations and predictions that informed our choices of laser crystal parameters.

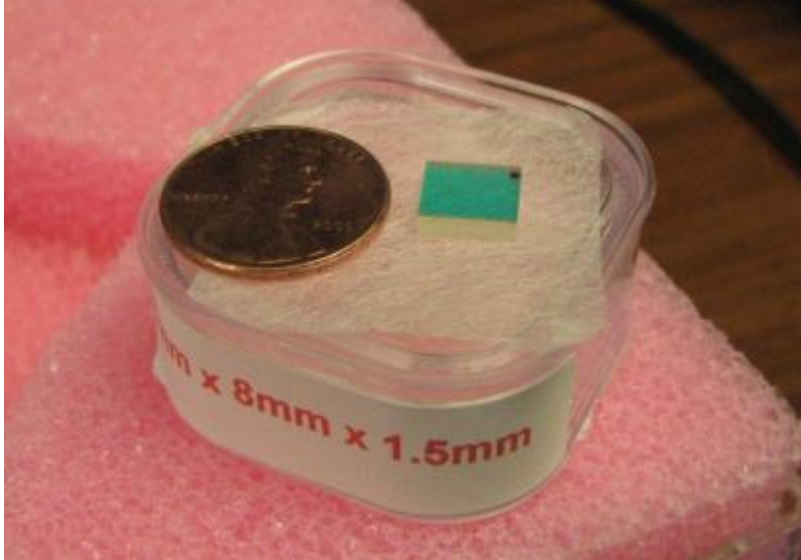


Figure 23: Photo of Tm:YAG crystal, 6% doping, 1.5 mm thick, AR coated.

3.4.2 Calculating Threshold

The lasing threshold condition for a laser resonator states that to be able to sustain stimulated emission (lasing), the round trip gain through the cavity must be greater than the total round trip losses. The lasing threshold is contingent on lasing material parameters as well as system parameters such as cavity length and end mirror reflectivity. The requirement on round trip gain may be expressed in terms of a threshold for absorbed pump power. In the literature, this is formulated by Mond [13] as:

$$P_{th} = \frac{h\nu_p}{\sigma_{abs}\tau} * \frac{V_m}{l} * \gamma \quad (3.2)$$

where ν_p is the pump frequency, τ is the upper state lifetime, l is the length of the cavity, σ_{abs} is the absorption cross section, V_m is the mode volume, γ is the total round trip loss coefficient.

For our calculations, we assume a $1/e^2$ intensity radius of 100 μm . For the cw design, there is no Q-switch in the cavity, so the length of the resonator is roughly the length of the gain medium, 2 mm. The loss coefficient γ is estimated at 5%, including mirror loss, scattering and any other passive losses experienced in the cavity. Using this information, we predict the threshold pump power to be on the order of 4.7 W.

3.4.3 Calculating Absorption

In the following plot we calculate theoretical power absorption in Tm:YAG crystals. We assume a 20 W pump beam with a mode diameter of 100 μm and a double-pass.

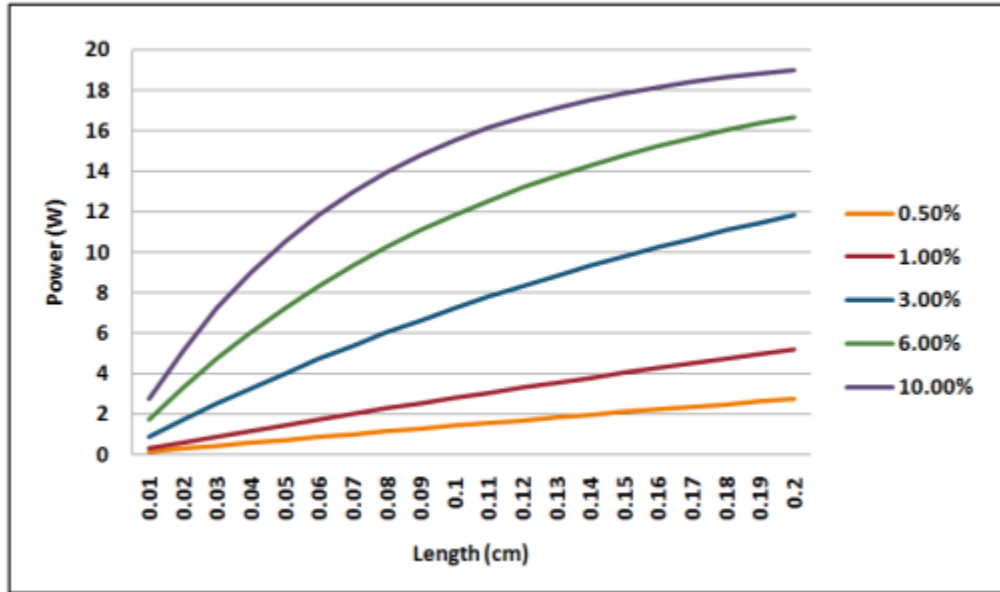


Figure 24: Plot of expected power absorption in Tm:YAG gain crystal assuming a 20 W pump beam. Different lines represent different doping percentages.

This plot was generated using Beer's law for absorption of optical radiation by a medium:

$$\frac{P_{out}}{P_{in}} = e^{-\alpha L} \quad (3.3)$$

where the P_{out} is unabsorbed pump power, P_{in} is input pump power, α is the absorption coefficient for the propagation medium and L is the length of the medium. The absorption coefficient was calculated using absorption spectra we gathered by testing our crystal samples in a spectrophotometer (see appendix A.3). The spectra were collected from the 6% doped Tm:YAG samples and were then scaled for the other doping levels. It is important to note that Beer's Law offers a somewhat limited picture of absorption as it only considers the most basic absorption and emission mechanisms. Depending on how strong the pump beam is, it is possible that we might saturate all available absorbers in the medium, though this is not something we expect to happen. There are also nonlinear absorption processes that may be considered: two-photon absorption by the YAG host and upconversion by the thulium ions. We have calculated that in the case of YAG, two-photon absorption will be negligible as the bandgap of YAG lies in the UV-VIS, which even two of our pump photons are not energetic enough to excite (Figure 25).

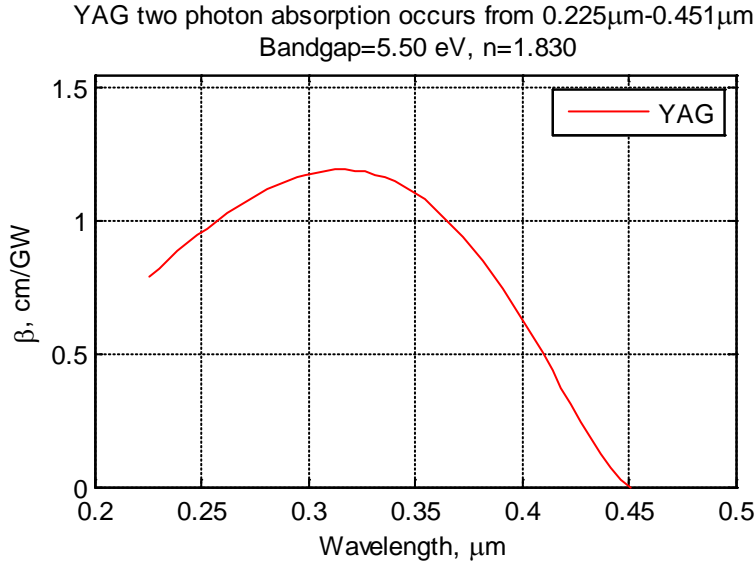


Figure 25: Two-photon absorption coefficient in YAG. Bandgap = 5.5 eV = 225 nm [28].

Upconversion, however, has previously proven to be a problem in Tm:YAG. Parasitic excitation of excited state Tm ions increases the state's upper laser level transition probability, which in turn shortens the state's lifetime and raises the threshold gain for the cavity. While this effect is documented in the literature [19], experimenters were still able to achieve laser operation by balancing pump intensity and upper-state lifetime.

When comparing Figure 24 to our actual crystals, we see that for our most strongly absorbing crystal (6% doping, 2 mm long) the most power we can expect to absorb from a 20 W pump will be around 17 W. When the same method is scaled to our 50 W pump laser, power absorption is near 45 W. We estimate that the threshold power of our cavity will be under 10 W (for a ~ 100 μ m spot size), so we expect no problems in getting the laser to turn on using this crystal. Furthermore, it appears that we may be able to reach threshold using a 6%-doped crystal as short as 0.25 mm or a 3%-doped crystal as short as 0.5 mm. Once laser operation is achieved, we should be able to scale back our system parameters significantly for optimum performance (for example, lowering pump power for better thermal management, shortening the gain medium for higher mode purity, etc.).

3.4.4 Dopant Level

Considering the relatively small stimulated emission cross section for Tm³⁺ ions ($\sim 5 \cdot 10^{-21}$ cm² [15]) and the inherently short active length of the microchip configuration gain medium, a high dopant percentage is desirable to ensure that the lasing threshold can be reached. However, having a doping percentage that is too high may actually raise the pump threshold due to an increase in nearest-neighbor parasitic upconversion processes (see section 2.2). While we were not able to perform a full quantitative assessment of the effects of doping percentage without actually having crystals in-hand, we were able to survey the literature and make reasonable predictions based on the outcomes of past experiments. The following table lists the doping levels and gain crystal geometries for several Tm:YAG lasers:

Table 8: Summary of published doping levels and gain medium geometries for Tm:YAG lasers.

Doping Level	Crystal Geometry	Reference
2%	Rod	[29]
3%	Rod	[15]
2%, 4%	Rod	[14]
4%	Rod	[19]
3%, 6%	Rod, Microchip	[27]
6%	Rod	[5]
10%	Microchip	[4]
12%	Microchip	[17]

It seems clear from this review that Tm:YAG laser crystals are typically highly-doped, on the order of 1-10% (atomic). Indeed, according to Honea *et al.* (1997), doping levels of at least a few percent are required for efficient cross-relaxation and therefore a quantum efficiency that approaches 2:1. Furthermore, even higher doping concentrations are used in the shorter laser crystal configurations, likely to offset thulium's low absorption cross-section.

Given our intention to use very short laser crystals, our large amount of available pump power, and our need to reach a high gain to overcome the losses associated with Q-switching, we chose to purchase Tm:YAG crystals in 6% doping, which is the highest dopant level we could find from any vendor without ordering a custom growth run. Crystals were also purchased in 3% doping, as this was available off-the-shelf from the same vendor and may be useful for comparison purposes or for operating with less severe thermal loading.

3.4.5 Cavity Modes

The phase condition for a laser oscillator states that, to avoid destructive interference in the circulating wave, a laser cavity may only support modes where the optical length of the cavity is an integer multiple of the mode's wavelength divided by two. Expressed mathematically, the number of modes that may oscillate in a cavity is given by:

$$N = \frac{2nL}{\lambda} \quad (3.4)$$

where L is the length of the cavity. Consequently, the frequency spacing of these modes is:

$$\Delta f = \frac{c}{2L} \quad (3.5)$$

or in wavelength:

$$\Delta\lambda = \frac{\lambda^2}{2nl} \quad (3.6)$$

So for a cavity length of 2 mm with a refractive index of 1.8 and a center laser wavelength of 2 μm , the modes that may oscillate are spaced by 75 GHz (or 5.7 nm at 2000 nm). In Figure 26, we plot this mode spacing against our intended Tm:YAG emission peak:

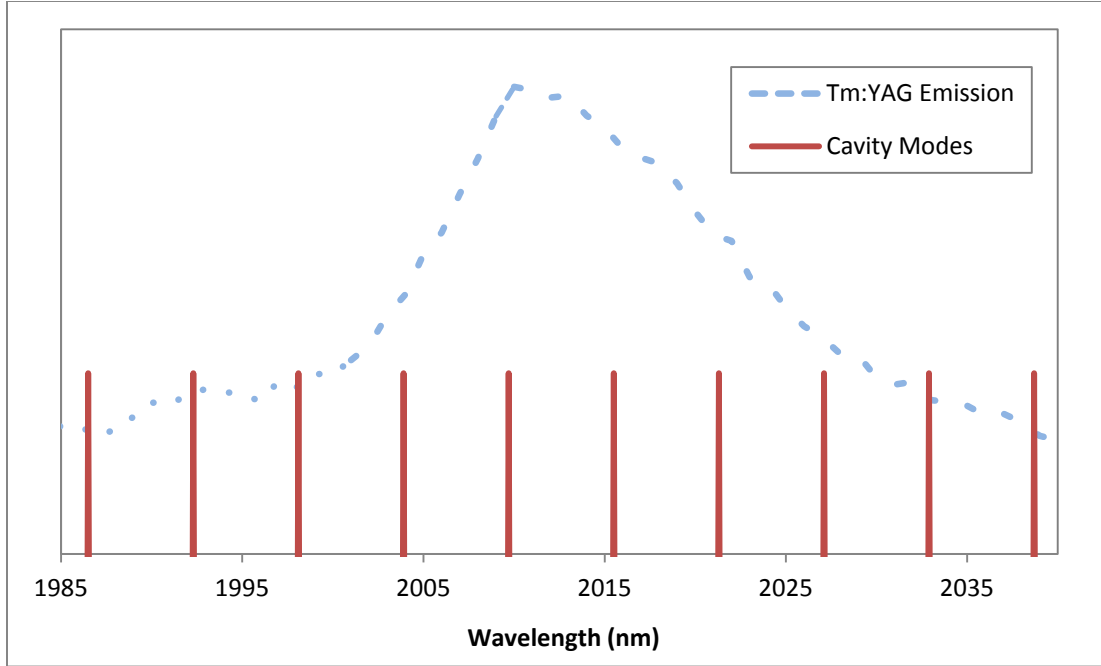


Figure 26: Cavity modes for 2 mm YAG crystal plotted along with Tm:YAG 2.01 μm emission peak.

It is difficult to predict exactly which modes will lase without knowing the full gain characteristics of the cavity. Ideally, only the one mode that is closest to the peak of the emission would oscillate, but given the density of cavity modes, this is unlikely to be the case in practice.

3.5 Thermal Lens

Thermal lensing is a refraction effect induced by temperature gradients in a medium. In all materials, the refractive index exhibits some dependence on temperature, typically quantified as dn/dT , which can be positive or negative depending on the material. In laser systems (especially high-power lasers), the gain medium is hotter in the region overlapping the laser mode than it is in surrounding areas, which creates a thermal gradient and in turn adds some convergence or divergence to the beam. While the magnitude of this effect is often difficult to calculate exactly, a relationship for a simplified rod laser is informative to mention here [30]:

$$f^{-1} = \frac{dn/dT}{2\kappa A} P_{heat} \quad (3.7)$$

This equation relates the effective focal length f of the thermal lens to dn/dT , the total heat dissipated P_{heat} , the area of the pump mode A , and the thermal conductivity κ .

Thermal lensing is typically an undesirable effect as it introduces instabilities into a system that can reduce beam quality and raise the pump threshold while being difficult to compensate for effectively. Steps taken to minimize the magnitude of thermal lensing can include pump beam shaping, cooling the gain medium, optimizing the geometry of the gain medium, etc. Indeed, the primary motivation frequently given for thin disk designs in the literature is mitigation of thermal effects [31].

That being said, in our particular system some degree of thermal lensing is desirable or even necessary. The plane/plane resonator design is inherently unstable as there is no focusing in place to confine the laser mode. Given that YAG has a positive dn/dT , the thermal lens effect will be positive, hopefully offering some degree of confinement and actually contributing to the stability of our laser system.

3.6 Active Q-Switch

For our active Q-switch, we needed a device that could achieve our target modulation rate of 1-5 kHz with a fast enough “opening” time as to not lengthen our pulses considerably, all while being as compact as possible in the interest of minimizing the overall cavity length. After searching through our available stock, we decided that the most appropriate choice was a custom model 10 W acousto-optic Q-switch from NEOS Technologies. These AO Q-switches are typically capable of modulation rates from DC to 100 kHz with RF rise and fall times on the order of 100 ns. Insertion losses are minimal and added length to the cavity was approximately 1.5 cm. The Q-switch was powered by a matched NEOS driver with a control signal from a BK Precision 10 MHz TTL function generator. This particular model needed to be cooled to under 45°C to function properly, so it was tied into the water-cooling loop for the Tm:YAG heat sink.

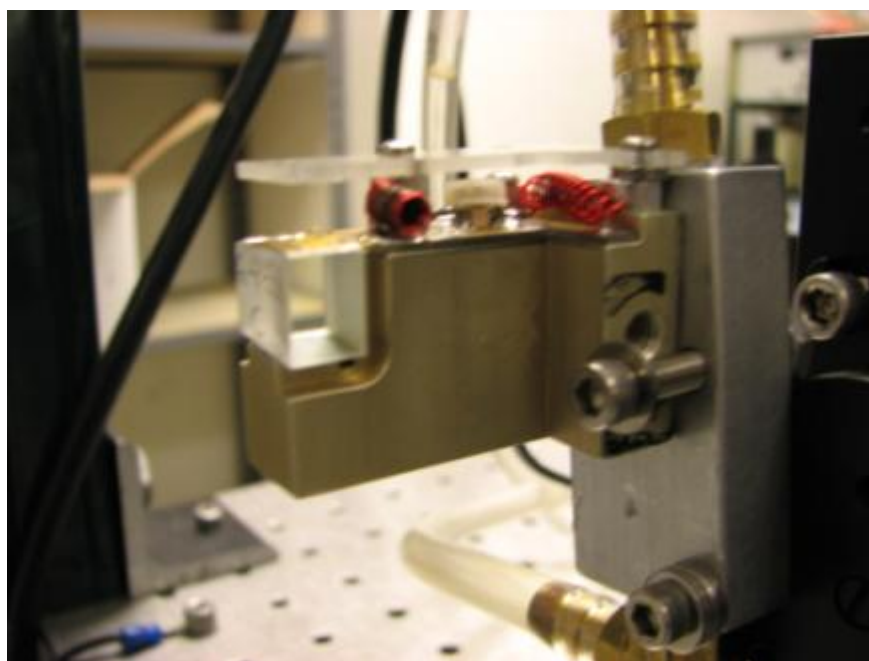


Figure 27: Photo of acousto-optic Q-switch used in experiment.

3.7 Heat Sinks

Given YAG's good thermal shock characteristics, removing all of the waste heat from the Tm:YAG crystal during laser operation was not a high priority. However, in order to minimize thermally-induced instabilities such as wavelength shifting, thermal lensing, etc., some cooling is needed to maintain a reasonably consistent temperature.

Our challenge in designing a heat sink for the Tm:YAG crystals was to find a way to mount the very thin crystals (as small as 0.1 mm thick) without breaking them or significantly reducing their clear aperture. Bracing the sides of the crystal could easily lead to fracture when subjected to thermal expansion. We were also constrained to a very narrow form-factor to keep the cavity as short as possible.

Our solution was to use a thin, flat piece of metal as the crystal mount to which we would adhere the crystal face with thermal compound. The crystal was mounted over a circular hole just smaller than the width of the crystal for the pump beam to pass through. The mount was attached to a water cooling block tied into a thermoelectric chiller. In Figure 28 and Figure 29 are a rough diagram of our first design and a photo of the completed heat sink (with mounted crystal).

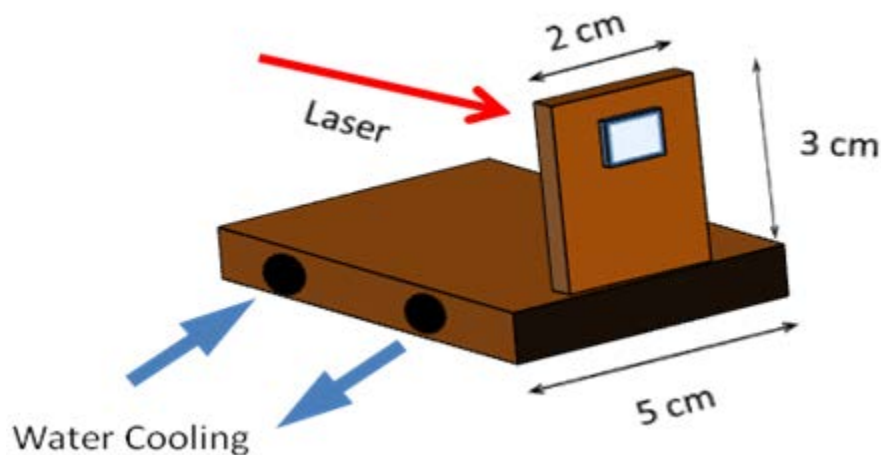


Figure 28: Rough diagram of original Tm:YAG crystal heat sink design.

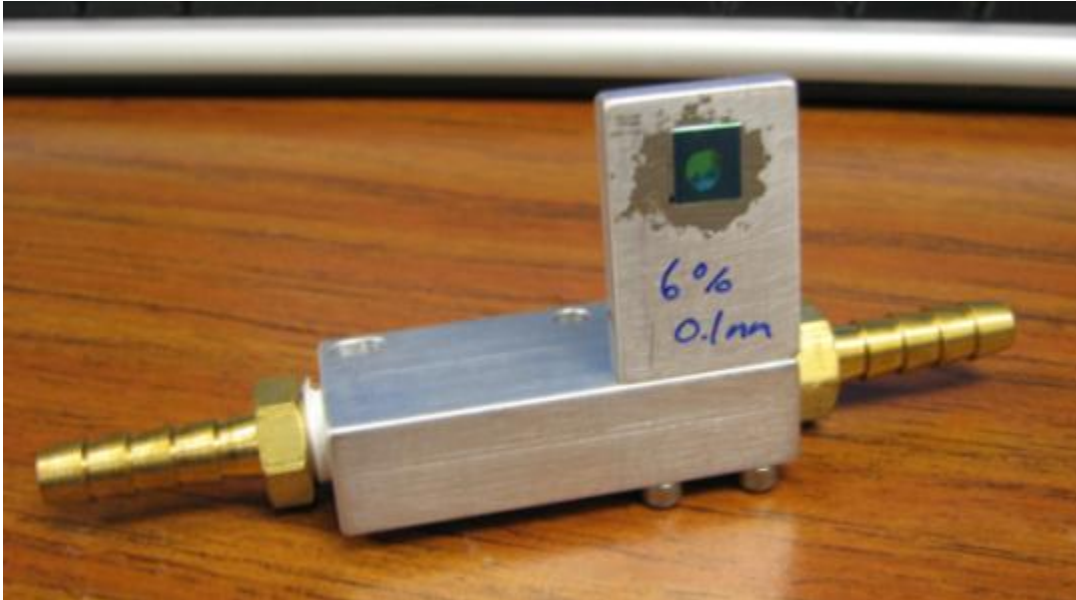


Figure 29: Photo of Tm:YAG heat sink, original design. Laser crystal is mounted using thermal compound.

Our design worked well as a heat sink for the crystal, but we eventually determined that the mount itself was too thick. Our focusing lens had a very short focal length (4 mm) and the thickness of the mount was preventing us from placing the crystal directly at the focus of the pump laser. In a second design, we replaced the mount with a thinned-down version. Additionally, the pump beam window was counterbored to fit over the focusing lens's mount, allowing us to focus the pump in the center of the laser crystal. A detailed diagram for the updated design may be seen in Figure 30.

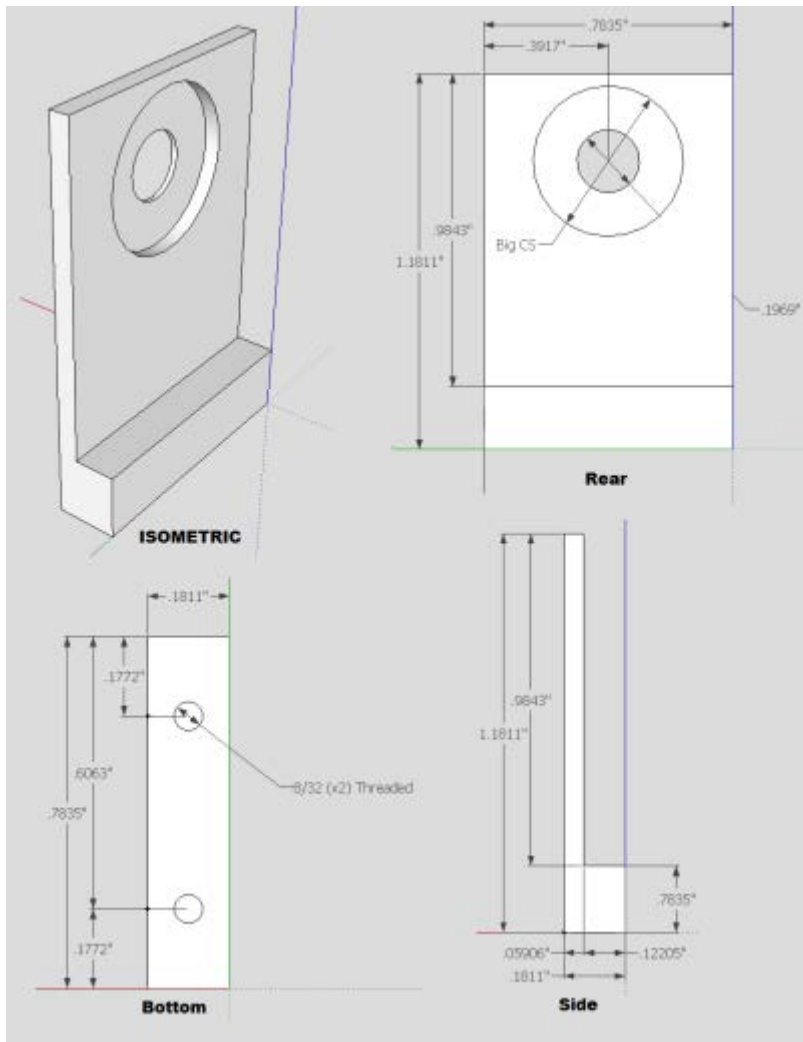


Figure 30: Detailed diagram for updated heat sink design. This version features a thinner mounting surface and a counterbored pump window to fit over pump lens mount.

3.8 Final System Design

The following figure is a diagram of our laser system in its entirety. Note that this is the actively Q-switched configuration; for the continuous configuration, the Q-switch is removed and the output coupler mirror is moved to within 1 cm of the Tm:YAG crystal.

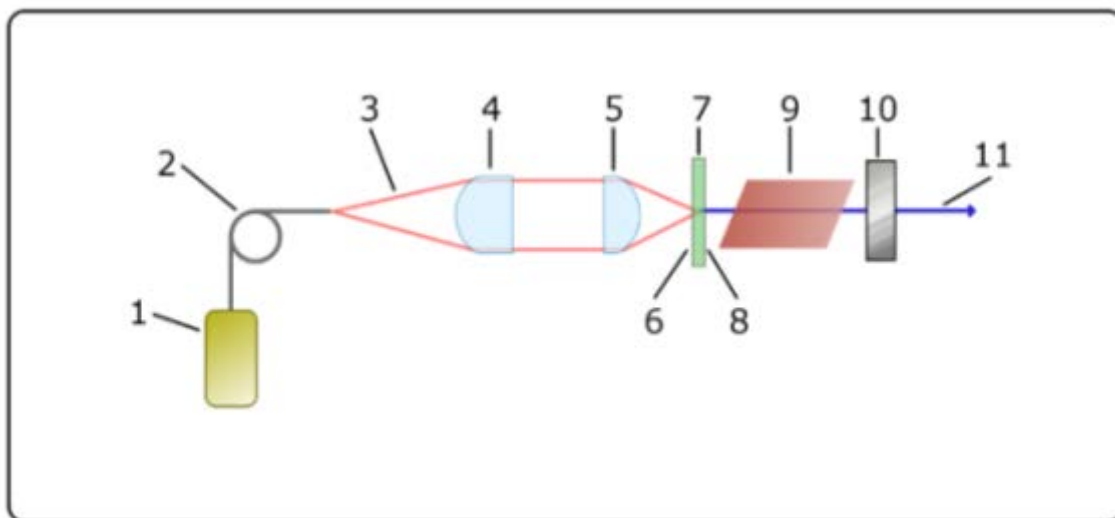


Figure 31: Schematic for actively Q-switched Tm:YAG resonator. 1) 785 nm pump laser, 2) pump fiber, 3) pump beam, 4) collimating lens, 5) focusing lens, 6) side 1 coating, AR @ 785 nm, HR @ 2000 nm, 7) 6% Tm:YAG crystal, 8) side 2 coating, AR @ 2000 nm, HR @ 785 nm, 9) AO Q-switch, 10) HR output coupler mirror, 11) laser output.

Chapter 4 – PASSIVE Q-SWITCHING

4.1 *Background*

As introduced earlier, Q-switching is a technique for pulsing a laser's output beam. There is a variety of methods used to produce this effect, but in all cases some device is inserted into the laser cavity to act as a variable attenuator and introduce additional losses to the cavity. While the laser is being pumped, the attenuation is first increased to the point that the cavity cannot reach its threshold gain (at which point the Q-switch is said to be "closed"), and then is rapidly decreased to immediately induce lasing (where the Q-switch is said to be "open"). Because the pumping has already created a population inversion in the gain medium, there is a large amount of stored energy available for forming a laser mode. This energy is released in a "giant pulse", which can often reach peak powers orders of magnitude greater than if the same cavity were operating in continuous-wave mode. After the pulse is released, the Q-switch is closed and the cycle repeats.

While we had some success using an active acousto-optic Q-switch (see section 5.6), the relatively slow speeds for this type of Q-switching gave us pulses longer than we would prefer. An alternative method for Q-switching that will likely produce shorter pulses (and is especially suitable for microchip and other solid state lasers) is to use a saturable absorber in the laser resonator. A saturable absorber is some medium, typically an optically-transparent crystal doped with an absorbing material, that has an absorption which decreases with increasing incident light intensity. As a result of this property, the saturable absorber can be used to Q-switch a laser cavity without requiring any external control ("passive" Q-switching). The process begins with pumping the laser medium and generating photons at the laser wavelength. Here, the saturable absorber is at its highest absorption, which means the cavity losses are also at their maximum. As pumping increases the number of circulating laser photons, the absorption of the Q-switch falls off until cavity losses are smaller than the gain and lasing begins. When the laser pulse is released from the cavity, circulation intensity drops and Q-switch absorption goes back up.

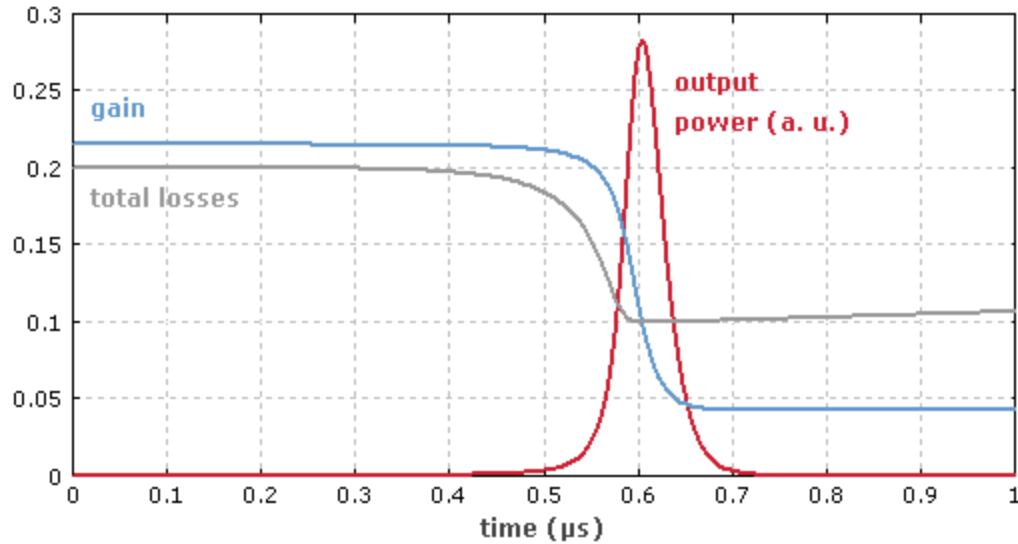


Figure 32: Temporal evolution of gain and losses in an example passively Q-switched laser. Shortly after the laser gain exceeds the resonator losses, a short pulse is emitted. Once the absorber starts to be saturated, the power rises rapidly [32].

The saturable absorber Q-switch is particularly well-matched to solid state lasers for a few reasons. Most apparently, it's a completely solid state device itself, which makes it both simpler and more robust than other methods of Q-switching. It is completely self-contained, requiring no external power source or modulation. The Q-switch crystal can often be bonded directly to the laser gain medium, or in some cases the gain medium itself can be doped with the absorbing material, combining gain and pulsing media into one device.

However, passive Q-switching comes with some considerable limitations that preclude it from being the best choice for all pulsing applications; most of these are consequences of device parameters that are fully dependent on the properties of the absorbing material and therefore offer limited adjustability after device fabrication. For example, the pulse rate of a passively Q-switched device cannot be changed without increasing the pump power, thereby increasing the spontaneous emission rate for laser photons and speeding up the saturable absorber's turnover time. This means the pump power cannot be changed without affecting the pulse rate. This is not necessarily the case with externally-modulated Q-switching devices. Furthermore, it may prove difficult to find an absorbing material for a wavelength of interest that has otherwise desirable properties. Finally, adding another photonic-active device to a laser system introduces additional phenomenological complexity, making predictive modeling more difficult.

4.2 Design

The most obvious consideration in designing a passive Q-switch is finding a material that absorbs strongly at the wavelength of interest; in our case, 2.02 μm . If the absorbing medium is being doped into a host crystal, it's also important that the host be transparent at that wavelength. We have decided that a good choice for Q-switching our Tm:YAG laser is chromium-doped zinc selenide (Cr^{3+} ion), because 1) our group has extensive experience with this material, and 2) Cr:ZnSe has been demonstrated to Q-

switch Tm:YAG lasers by Tsai and Birnbaum [5]. In the following figure we can see that Cr:ZnSe exhibits significant absorption at the laser wavelength (the exact magnitude of absorption will vary with the sample dopant level).

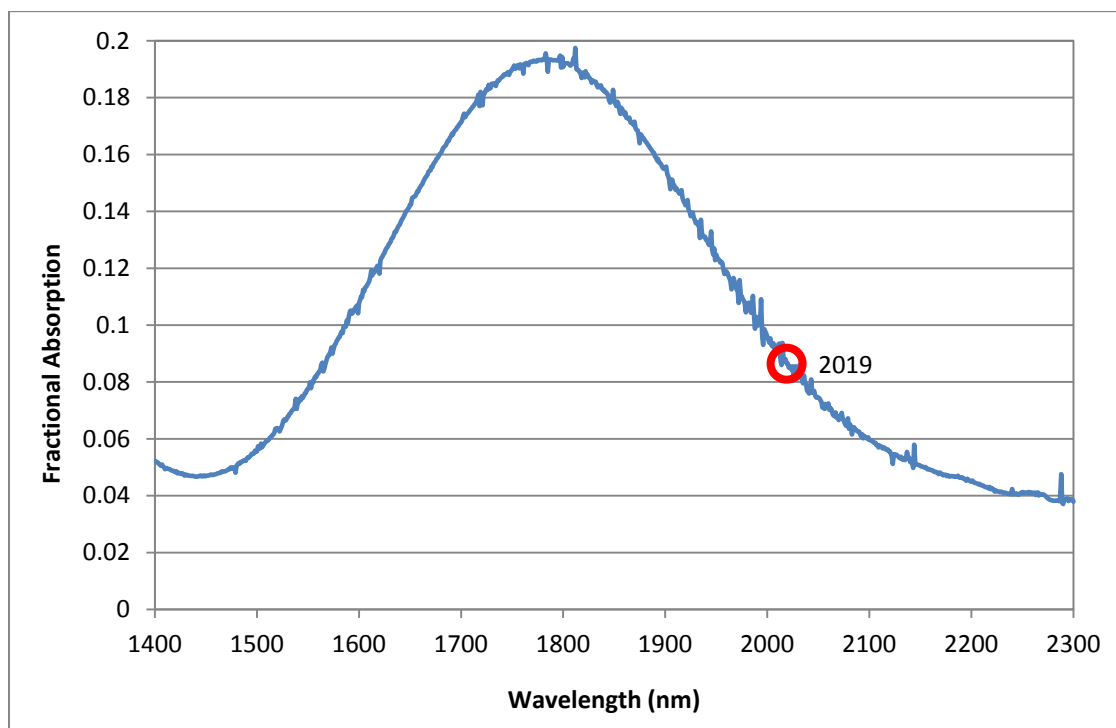


Figure 33: Absorption spectrum for Cr:ZnSe sample collected with Cary 5000 spectrophotometer. Sample was AR coated for all wavelengths shown.

The chief difficulty in designing a passive Q-switch is choosing a doping level for the absorbing ion that is appropriate for a particular laser cavity. Here it is useful to discuss doping level in terms of *small signal* or *initial* transmittance, or the fraction of the beam which passes through the saturable absorber crystal before the crystal has begun to saturate. Also relevant to our discussion is the final transmittance: the transmittance when the crystal is fully saturated.

If the initial transmittance is too high, the losses introduced to the cavity won't be great enough to raise the lasing threshold and the laser will simply run in continuous wave mode. If it is too low, the added losses will be too great to overcome – the crystal won't be saturated and the laser won't run at all. To choose an initial transmittance you must know how much additional passive loss a cavity can tolerate before it is no longer capable of reaching threshold. The total unsaturated loss must be above this value while the total saturated loss must be below it.

The passive loss that may be withstood by a laser can be determined by gradually adding more and more loss to a functioning cavity until it ceases to run. For example, we were able to run our Tm:YAG laser with 99.9, 98, and 96% reflectivity output couplers, but were unable to run it at 90%. This suggests that, with the 99.9% mirror in place, our final transmittance must be no less than 90-96%. Our initial transmittance must be less than that, but it can't be so low (which is to say, the doping

can't be so high) that the saturation irradiance of the crystal is greater than what the laser can produce.

To find the maximum circulating intensity in the cavity, we look to our results from section 5.2. It seems that our maximum output power achieved before thermal roll-off was on the order of 450 mW. This data was collected with a 96% reflectivity output coupler, so we can deduce that the power circulating in the cavity was approximately 11 W. We will assume that the laser mode diameter is roughly equal to the beam diameter as it exits the output coupler, which is about 1 mm. This means that our maximum intracavity irradiance is going to be somewhere between 10^5 and 10^6 W/cm².

Our lab has a collection of chromium-doped zinc selenide samples from previous experiments. The following figure is a plot of transmittance versus incident irradiance for several of these samples.

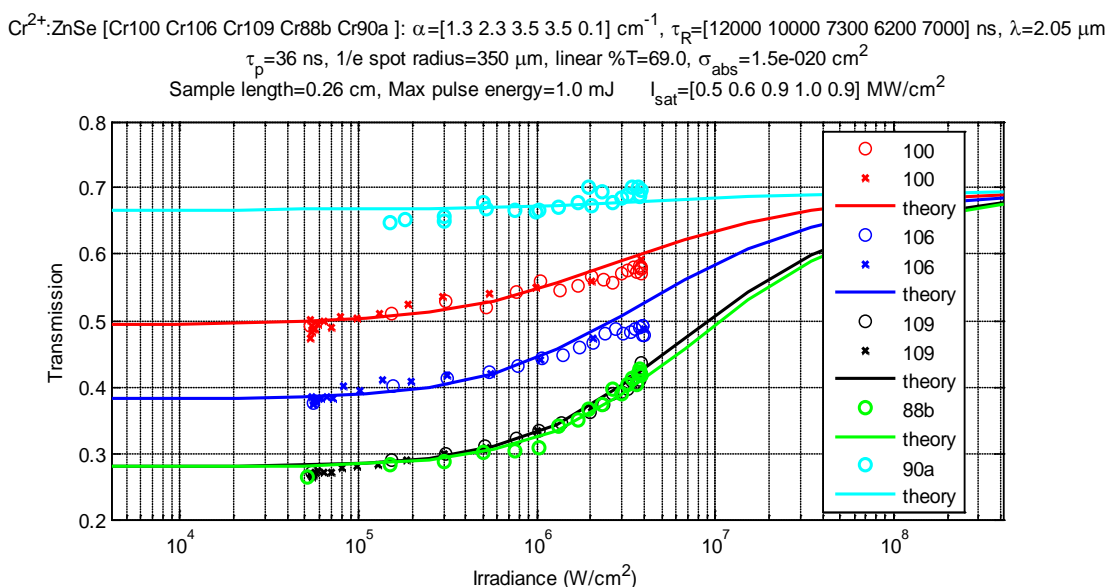


Figure 34: Transmission as a function of incident irradiance for several Cr:ZnSe samples [28].

By displaying the data in this manner, the saturation behavior of the samples becomes evident. We had initially hoped that we might be able to use one of these samples to Q-switch the Tm:YAG laser. However, it is clear from the above plot that this is not feasible. In order to reach a state of saturation, we would require an incident irradiance of 10^9 W/cm², but we have established that our intracavity intensity is likely to be between 10^5 and 10^6 W/cm². Furthermore, Figure 33 shows us that the baseline losses in a crystal such as these are on the order of 5%. This is too lossy for our cavity, which we have determined may only sustain an additional 4-10% of additional passive loss. To Q-switch our cavity, a crystal will need to have a much lighter doping.

4.3 Modeling

To determine precisely what level of doping would be optimal for our laser, we can model the behavior of a saturable absorber exposed to incident radiation. In the following discussion we outline a method for numerically solving the set of atomic rate equations associated with a Cr:ZnSe saturable absorber crystal. The equations are based on Cr:ZnSe amplifier equations defined previously by Berry [33].

We want to determine the saturable absorber crystal's transmittance as a function of incident intensity. We start by defining the intensity differential equation for the transition of interest in Cr:ZnSe:

$$\frac{\partial I}{\partial z} + \frac{1}{v} \frac{\partial I}{\partial t} = -\sigma_{abs} I n_g + \sigma_{em} I n^* \quad (4.1)$$

The only two mechanisms significant enough to include in this discussion are ground state absorption (right-hand side, first term) and excited state emission (right-hand side, second term). Because the saturable absorber Q-switch typically “opens and closes” on a very fast time scale compared to other processes in a laser cavity, we will assume a steady-state solution, implying the variation of intensity with respect to time is negligible. The differential equation for excited state population with respect to time is:

$$\frac{dn^*}{dt} = \frac{1}{h\nu} (\sigma_{abs} I n_g - \sigma_{em} I n^*) - \frac{n^*}{\tau} \quad (4.2)$$

We may also enforce conservation of population:

$$n_t = n^* + n_g \quad (4.3)$$

Again, since we are pursuing a steady-state solution, we will assume time variation of the excited state population to be zero:

$$0 = \frac{1}{h\nu} (\sigma I [n_t - n^*] - \sigma_{em} I n^*) - \frac{n^*}{\tau} \quad (4.4)$$

This allows us to solve the equation for n^* . This is one of the two equations that will be used in our numerical solver:

$$n^* = \frac{n_t \sigma_{abs}}{\frac{h\nu}{\tau I} + \sigma_{abs} + \sigma_{em}} \quad (4.5)$$

Now back to the differential equation for intensity, which we can simplify to:

$$\frac{dI}{dz} = n^* I (\sigma_{abs} + \sigma_{em}) - \sigma_{abs} I n_t \quad (4.6)$$

Expressed as a numerical approximation, we are left with the second equation for the solver:

$$\Delta I = [n^* I (\sigma_{abs} + \sigma_{em}) - \sigma_{abs} I n_t] * \Delta \quad (4.7)$$

where Δz is the step size along the length of the crystal. To solve the equations with a computer, we program a step solver to alternate between evaluating the previous

expression and the expression for n^* for steps of Δz , keeping track of the intensity as a function of length with the expression:

$$I_1 = I_0 + \Delta \quad (4.8)$$

When the solver has finished running, we have a plot of intensity in the crystal as a function of the crystal's length. For example, the following figure is an intensity profile for a 2 mm long, lightly-doped Cr:ZnSe crystal (Figure 35):

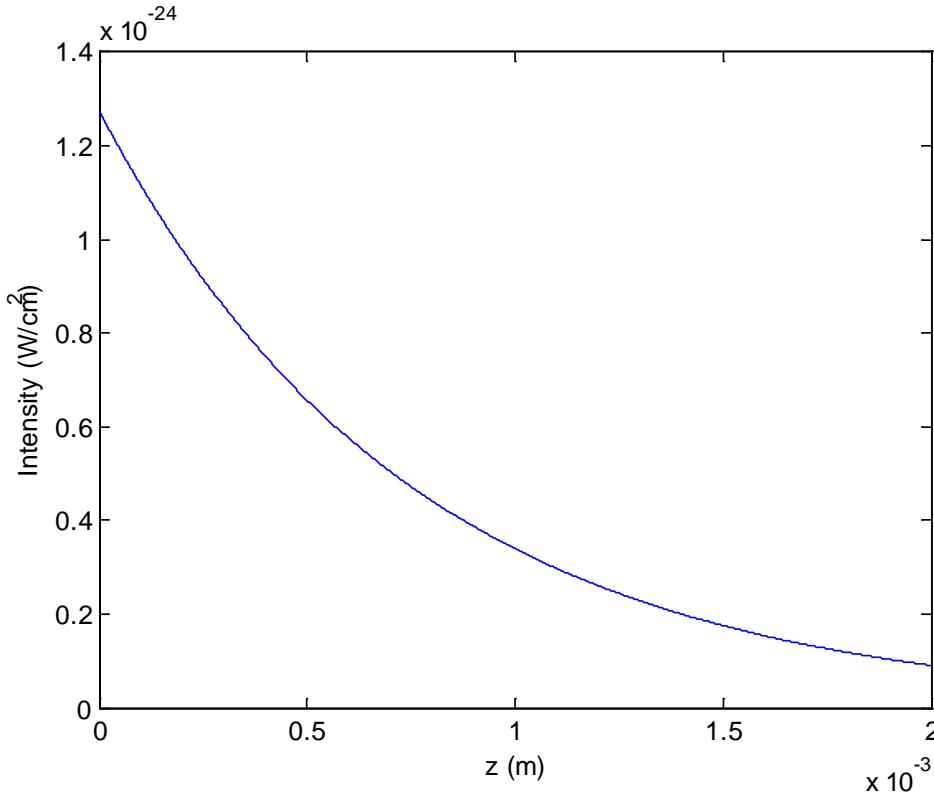


Figure 35: Intensity of signal beam through the length of a SAQS crystal.

By dividing the intensity at the output face by that at the input face, we obtain a value for the crystal's power transmittance at the selected intensity. By repeating this process over a range of intensities, we are able to produce a plot of transmittance vs. incident intensity, helping us to predict the saturation behavior of a particular crystal (Figure 36). This crystal is 0.25 mm long and is doped with 5×10^{24} chromium ions per m^3 , which corresponds to an atomic doping of 0.0221%. The diameter of the incident beam is 1 mm.

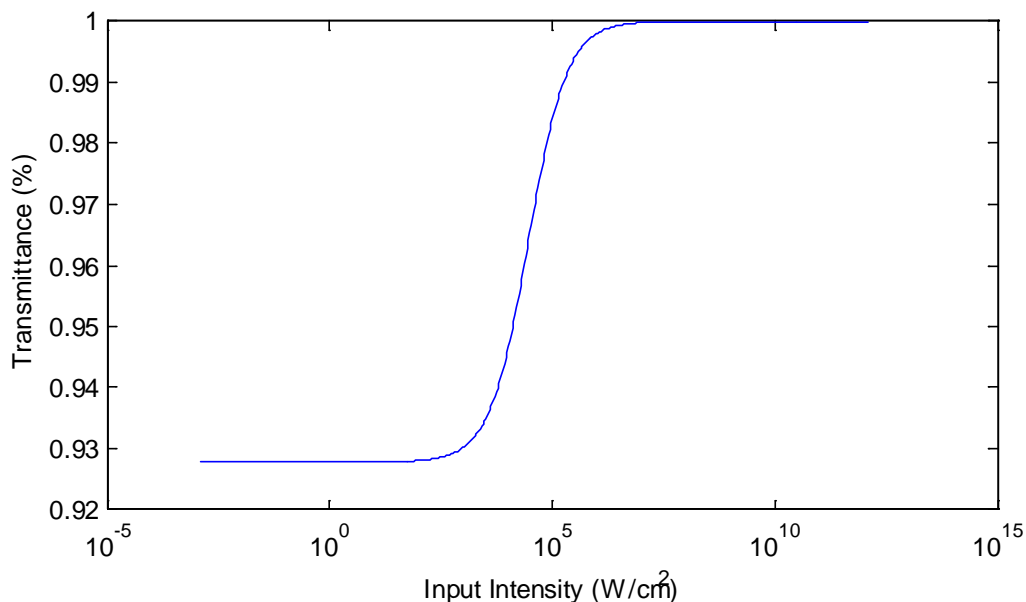


Figure 36: Logarithmic plot of transmittance vs. incident irradiance for a SAQS.

From this plot, it seems likely that a saturable absorber crystal of these parameters could work to Q-switch our laser. The unsaturated loss is between 4 and 10%, as stipulated previously (saturated loss has been ignored for this calculation). Furthermore, the saturation irradiance of $\sim 10^5$ W/cm² falls within our expected range for intracavity intensity. Knowing this, our best strategy for maximizing our chances of experimental Q-switched operation is to have several Cr:ZnSe samples fabricated in a narrow range of dopant percentages near 0.02%, or alternatively, a single long sample with a dopant gradient that may be translated through the beam path to find the ideal dopant level.

Experimental passive Q-switched operation was attempted, but not achieved, with two saturable absorber samples: an AR-coated, chromium-doped zinc sulfide sample with an initial transmittance of 93%, and an AR-coated chromium-doped zinc selenide sample with 91% initial transmittance. We suspect that both of these samples were too highly-doped to be saturated by our laser system.

Chapter 5 – LASER PERFORMANCE AND CHARACTERIZATION

5.1 First Attempt and Subsequent Thermal Damage

The original construction of the Tm:YAG resonator used a 0.25 mm long, 6%-doped crystal as opposed to the 2 mm long piece that has been discussed more extensively in this report. With an available 40 W of pump power and our calculations on pump absorption (see section 3.4) we were optimistic that we would be able to meet the lasing threshold with this shorter crystal. The cavity was constructed with a 92% reflectivity output coupler in place and roughly aligned using a helium neon laser. We conducted several trials of making fine alignment changes to the end mirrors to get the system to lase, increasing the pump power each time, which eventually brought us to our maximum pump power of 40 W. At this point the Tm:YAG crystal sustained significant damage, shown in the following images.

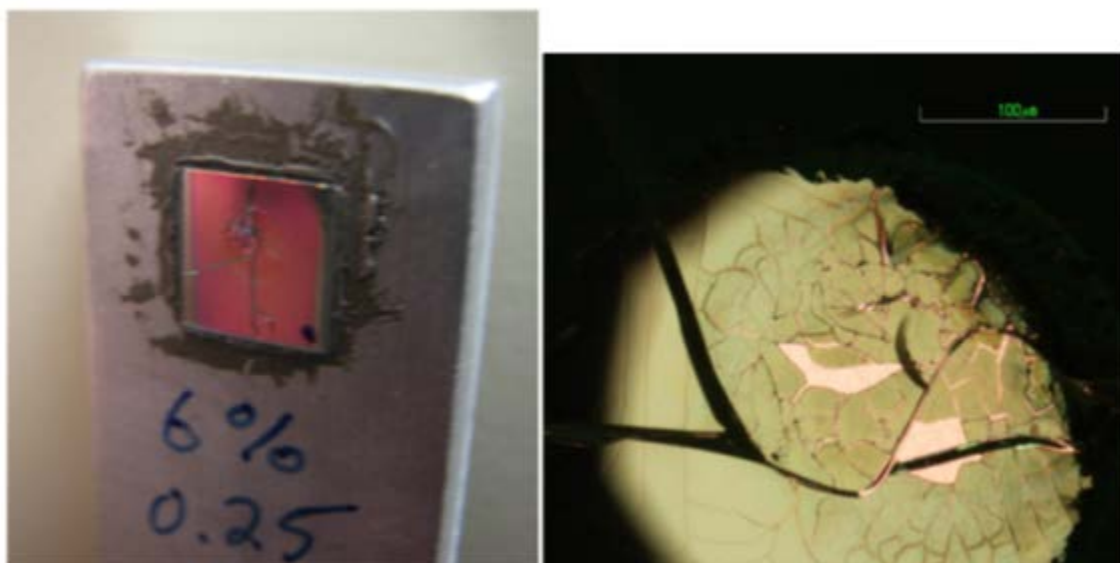


Figure 37: Macroscopic (left) and microscopic (right) photos of thermal damage in Tm:YAG gain crystal.

To help understand the mechanism of damage, we constructed a model of the laser crystal and the cooled mounting plate using COMSOL finite element analysis software. Figure 38 shows a YAG crystal mounted to a ring-shaped heat sink with a tightly focused pump beam incident. It is visible from this image that any thermal damage sustained was not a failure of the heat sink itself, as it and even the outer edges of the crystal itself are still at reference temperature. The problem is that the small and intense beam creates a very steep thermal gradient across the crystal, one that the crystal itself is not conductive enough to even out in thermal equilibrium. This stark difference of temperatures within the crystal is what creates the stress that leads to cracking.

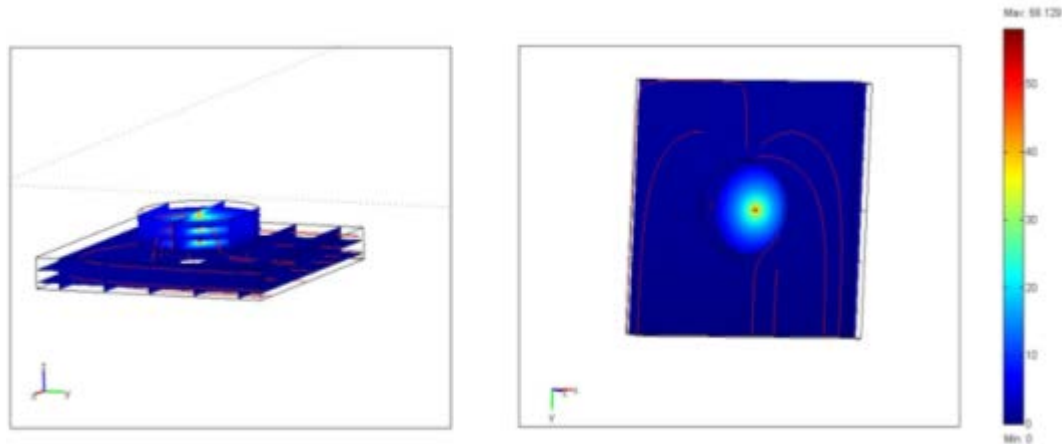


Figure 38: Thermal modeling of Tm:YAG crystal and mount, side view (left) and front view (right), pumped with 40 W of power. Temperature scale is relative to cooling block temperature (15°C).

This is not a problem that could have been solved with a more conductive heat sink. Other cooling methods may have been helpful, such as one that incorporated convective cooling in addition to conductive, but the simplest solution was to use thicker crystals to increase absorbed pump power while staying below the thermal fracture point. For example, by using a crystal twice as long, we would be able to absorb twice as much pump power but keep the absorbed power density the same, thus staying below the damage threshold. Of course, in lengthening the crystal there were compromises made in terms of spectral purity and eventually pulse width, but we were at least able to get the system to run.

5.2 Output Power and Slope Efficiency

For the second iteration of the laser system, the 6%-doped, 0.25 mm crystal was replaced with a 6%-doped, 2 mm long crystal, while the 92%-reflectivity output coupler mirror was replaced with a 98% reflectivity output coupler mirror. Figure 39 is a plot of the Tm:YAG laser's output power versus pump power. The laser was pumped by the nLight Pearl diode laser running at 785 nm. The overall cavity length was less than 1 cm.

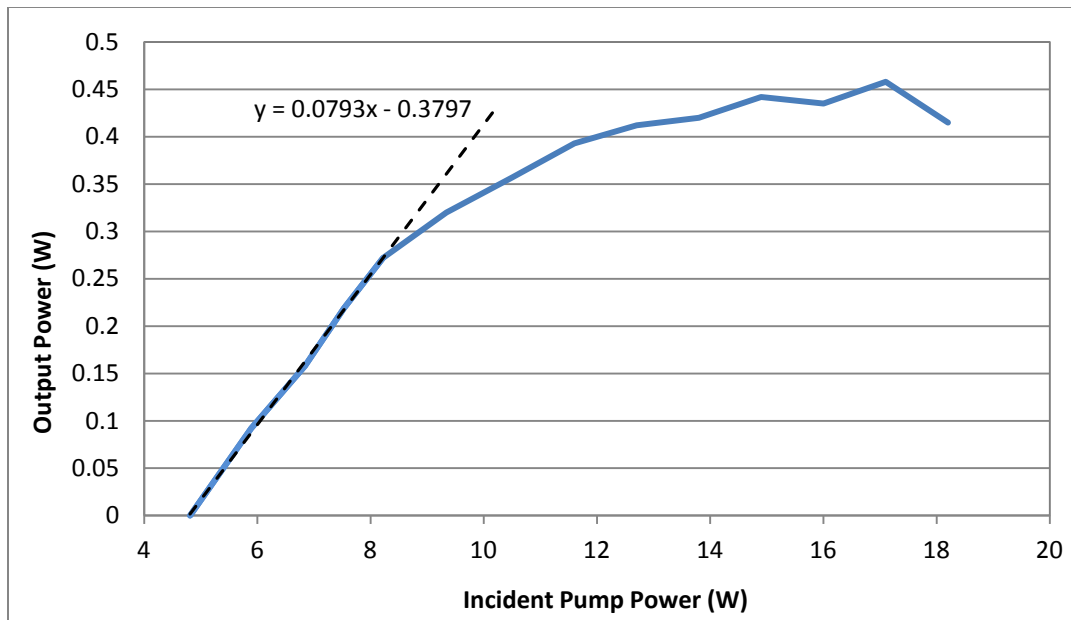


Figure 39: Output power vs incident pump power for Tm:YAG laser.

From the plot it is clear that the threshold for incident pump power is 4.8 W with a slope efficiency of 7.9% -- when pump absorption is accounted for, these values are closer to 4.0 W and 9.5%. This is starkly different than the efficiencies as high as 50% reported in the literature. However, we must stress here that our resonator was not built for high efficiency. Our choice of a high reflectivity output coupler, which was chosen to minimize the lasing threshold, has been shown to reduce slope efficiency drastically [14]. The slope efficiency was measured for two additional output coupler mirrors, and the results follow the expected trend of reduced efficiency with higher reflectivity (Figure 40).

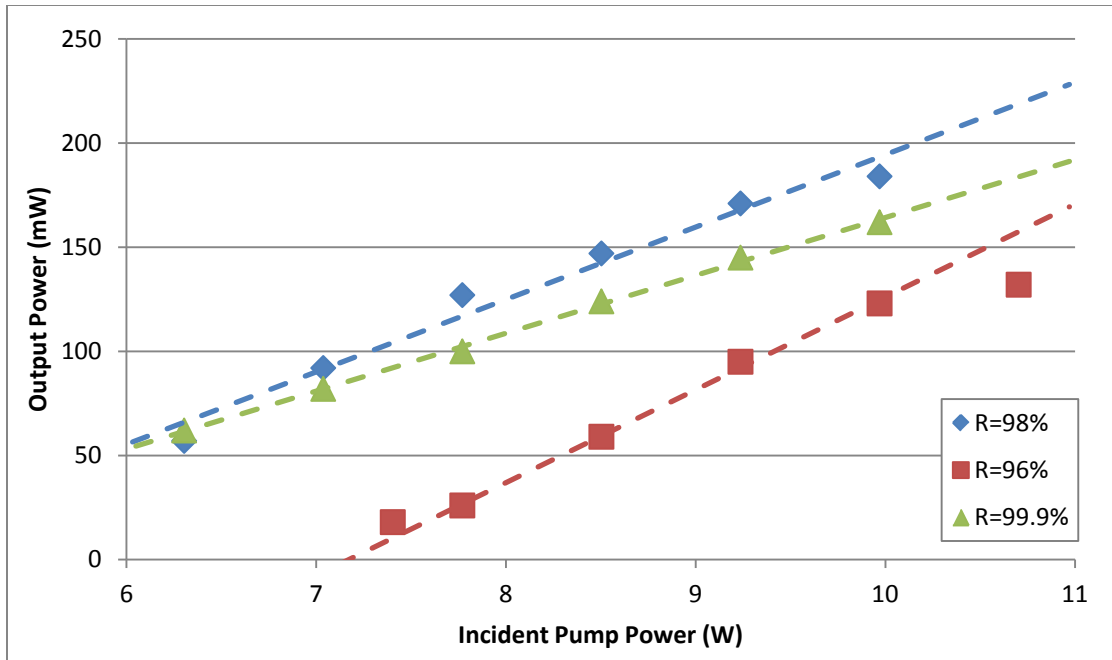


Figure 40: Slope efficiency of Tm:YAG laser cavity for output coupler mirrors of varying reflectivity.

The other pertinent feature of Figure 39 to be considered is the curvature taken on after the linear region and the fluctuation that follows. This behavior is almost certainly due to thermal lensing: as more heat is absorbed, the thermal lens becomes more severe and the overlap of the pump and laser modes worsens, resulting in rapidly diminishing returns on increased pump power. Eventually, output power levels off completely and begins fluctuation with the growing thermal instability. This puts significant limitations on our laser performance as all of the additional pump energy (which the laser crystal itself is capable of absorbing) goes to waste.

5.3 Findlay-Clay Analysis

Findlay-Clay analysis is a technique developed to measure the passive losses in a laser cavity by comparing the laser's slope efficiencies for at least three different end mirror reflectivities [34]. Knowing the total loss in a laser resonator is valuable for assessing the quality of a system's design and identifying where there is room for improvement. More specifically, it helps us to determine how much additional loss can be accommodated from adding a Q-switch to the cavity.

We have collected slope efficiency data for our cw Tm:YAG laser resonator using output coupler mirrors of three different reflectivities. Output power vs. pump power was measured for 96, 98, and 99.9% reflectivity output coupler mirrors. The range of pump powers used in measurement was deliberately kept narrow to minimize the effects of temperature variations in the diode. The cavity was pumped only a few watts above threshold to avoid thermal lensing. Results may be seen in Figure 40.

The slope efficiencies decrease with decreasing output coupler reflectivity, which is the expected trend. If the fit lines for the Figure 40 are extrapolated to the point of zero output power, we can find the threshold pump power at the x-axis crossing.

Plotting the threshold pump power against the negative natural log of output coupler reflectivity is shown in Figure 41:

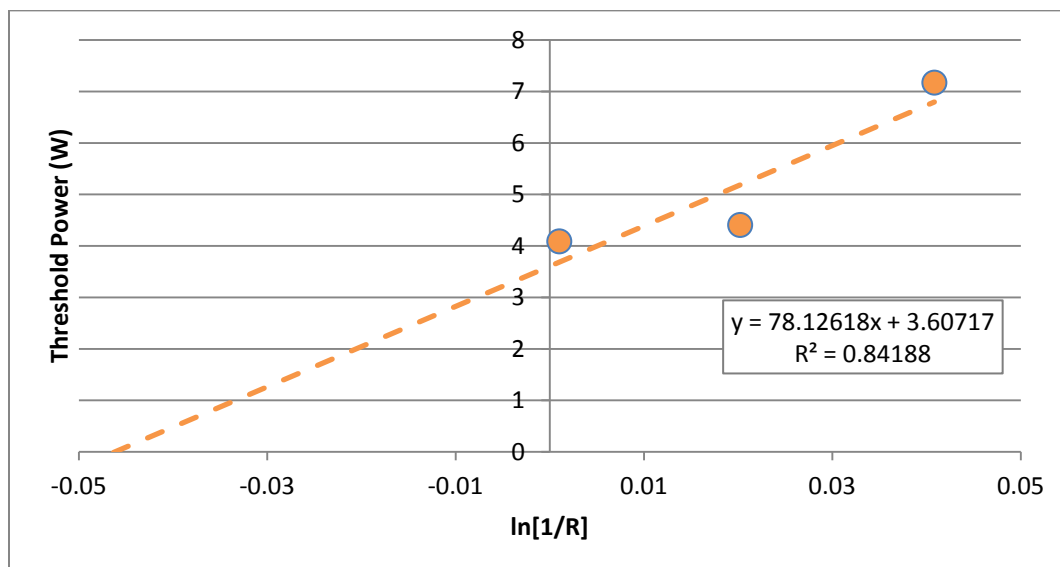


Figure 41: Threshold pump power vs. output coupler reflectivity for Tm:YAG laser cavity.

These three points form a line that can then be interpolated back to the x-axis crossing. The magnitude of the resulting x-axis offset gives an estimate for passive losses in the cavity -- in this case, $4.6 \pm 2.2\%$. Clearly there is a high degree of uncertainty in this linear fit, due to factors such as small variations in cavity length, temperature instabilities, non-optimal alignment, etc., but this result confirms our expectation that passive losses for the cavity would be relatively high compared to microchip laser resonators using better-established materials such as Nd:YAG. This is an important piece of information for characterizing the cavity and determining an appropriate small signal transmission for the saturable absorber Q-switch.

5.4 Spectral Content

An output spectrum for the Tm:YAG laser was collected with a Yokogawa AQ6375 optical spectrum analyzer. The laser was run in continuous mode, pumped by the Bright Solutions diode laser with 10 W at 780 nm and with a 99.9% reflectivity output coupler mirror. OSA resolution was set to 0.1 nm in Figure 42 and 0.05 nm in Figure 43 with a 500 frame averaging filter.

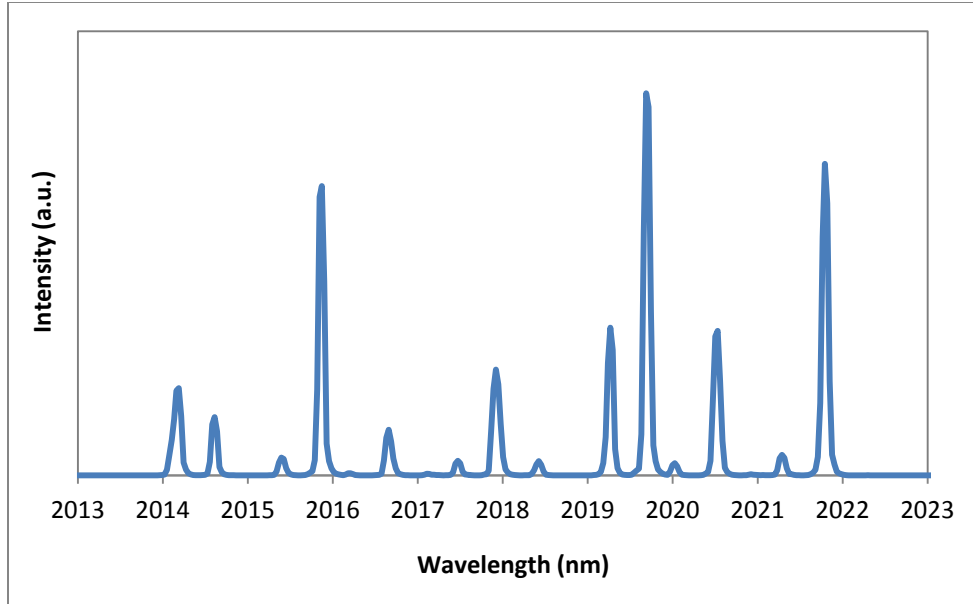


Figure 42: Full output spectrum for Tm:YAG laser. Vertical axis is linearly scaled.

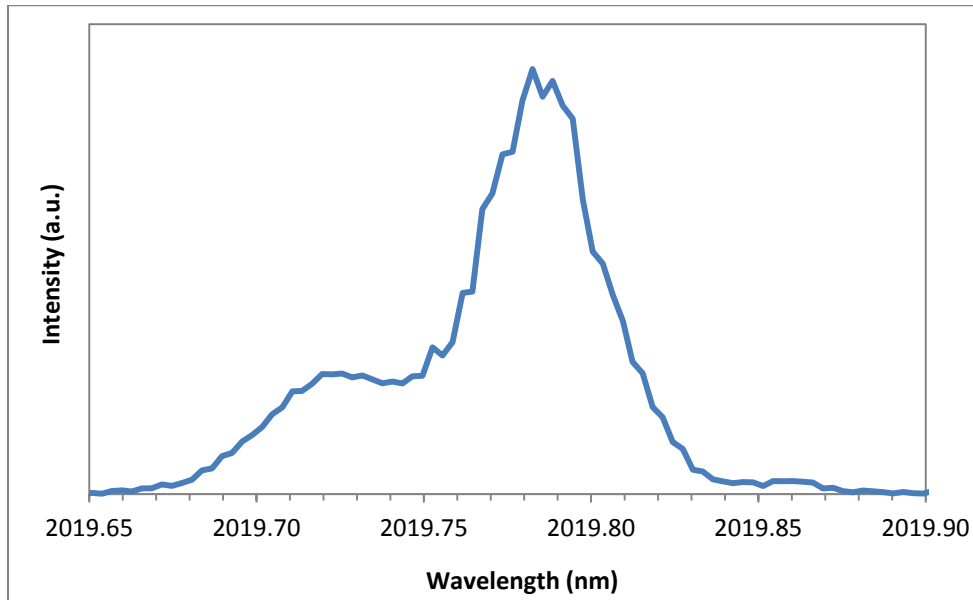


Figure 43: Largest peak of output spectrum for Tm:YAG laser. Vertical axis is linearly scaled.

The peak emission wavelength of 2019.78 nm with a full-width half-max of ≤ 0.045 nm is consistent with what we expected for this laser, though while we predicted multimode operation, the additional modes are unexpectedly strong. The ~ 0.5 nm mode spacing corresponds to a cavity length of 2 mm, suggesting that there is some etalon-like resonance taking place in our 2 mm-long gain crystal. This most likely indicates that the $2\text{ }\mu\text{m}$ anti-reflective coating on the gain crystal is not as effective as we had hoped.

5.5 Beam Profiling

The following beam profile was collected with the Tm:YAG laser running in continuous mode at about 170 mW of output power. The laser was pumped with the Bright Solutions diode laser running at 780 nm, the output coupler used was ~99.9% reflectivity and the cavity length was made as short as possible (~1.5 cm). A Photon Inc. Nanoscan scanning slit beam profiler was used for the measurement. The scan rate was set to 10 Hz with a 25-frame averaging filter. To ensure that the beam had a well-defined waist, it was focused using a 7.5 cm focal length lens. Neutral density filters were used to attenuate the beam to an appropriate intensity for the profiler. Beam waist was measured every 0.5 cm away from the waist and every 0.2 cm near the waist. To assess the beam quality, profiles were fitted to Gaussian distributions.

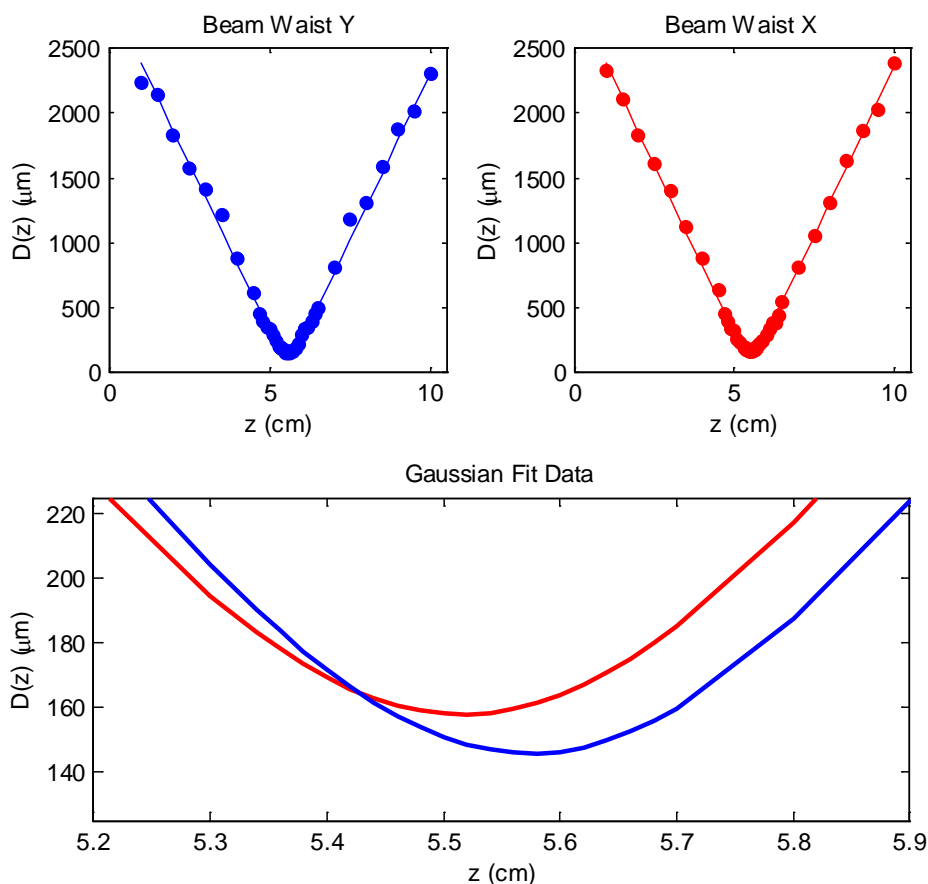


Figure 44: Output beam profile for Tm:YAG laser. The upper left and upper right plots show beam waist (in vertical and horizontal dimensions, respectively) as a function of propagation distance, while the bottom plot shows Gaussian fits to the aforementioned beam waist plots.

The beam was mostly circular and uniformly divergent as shown by the plot. We determined that the beam quality was $M^2 = 8.7$ in the x-dimension and 10.5 in the y-dimension. This is consistent with what we would expect for a multimode solid-state laser.

5.6 Pulsed Performance

An AO Q-switch was inserted into the cavity (see Figure 31) to investigate the laser's pulsed performance. Figure 45 shows an example pulse from the actively Q-

switched Tm:YAG laser. The process for converting the laser from continuous to pulsed was as follows: The cw cavity was turned on using the 99.9% output coupler. Once lasing was achieved, the cavity was gradually lengthened enough to accommodate the acousto-optic Q-switch. With the Q-switch put into place, cw operation was again confirmed, then the Q-switch driver was turned on. Pulses were measured using a photodiode and were found to have a duration of approximately 400 ns. The average power was 42 mW and the pulse frequency was 1.66 kHz, giving a pulse energy of 25 μ J. Pump power was 10 W at 785 nm from the Bright Solutions diode laser.

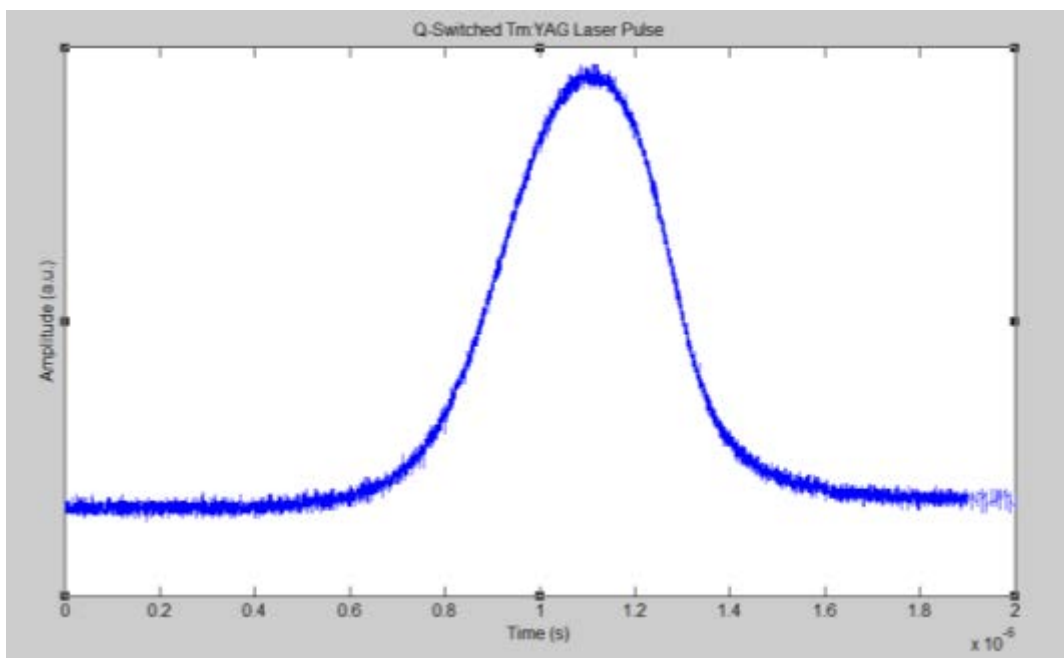


Figure 45: Example of pulsed output from actively Q-switched Tm:YAG laser. Pulse width is approximately 400 ns.

It was very difficult to get the laser to run in Q-switched mode. Even continuous operation was extremely sensitive while the cavity was being lengthened to accommodate the AO Q-switch. Once the Q-switch was in place and turned on, fine adjustment was required for the laser's control parameters as well as the spatial orientation of the AO crystal before uniform pulsing could be achieved. For this reason, we were unable to collect the data for a more detailed characterization of Q-switched operation, such as an output versus input power curve. We were also unable to reduce the output coupler reflectivity to optimize for pulse duration, as this would have raised the lasing threshold and rendered pulsed output unattainable.

This highly unstable operation is most likely a result of the plane-plane resonator configuration. With the weak mode confinement of a plane-plane system, any lengthening of the cavity makes it far more difficult to hold the plane mirrors parallel enough to sustain resonance. This problem could be solved by using a converging output coupler mirror whose focal length is matched to the length of the cavity.

Chapter 6 – CONCLUSIONS AND DISCUSSION

6.1 Conclusions

In this thesis we have detailed the design, modeling, construction, and operation of a diode-pumped, solid state, actively Q-switched microchip laser operating at 2 μm using Tm:YAG as the lasing medium. The maximum output power achieved thus far is 450 mW with a slope efficiency of 9.5%. The laser's output was multimode with a center peak at 2.019 μm . The linewidth was ≤ 0.045 nm. Using an acousto-optic Q-switch, the laser was run in pulsed mode at an average power of 42 mW and a pulse rate of 1.66 kHz. Pulse duration was approximately 400 ns with a pulse energy of 25 μJ .

6.2 Future Work

There are a number of additions and improvements to this laser system that we have considered to contribute to operational stability, ruggedness, spectral purity, or shortening of pulse duration. Some we plan on implementing in the near future while others serve longer-term interests.

6.2.1 Passive Q-Switch

In the nearer term, our first concern is to replace the active Q-switch with a Cr:ZnSe saturable absorber passive Q-switch, the design of which we have discussed previously in section 4.2. As we have found that it is difficult to determine appropriate saturable absorber transmittance properties from simulation alone, we plan to purchase either several samples of Cr:ZnSe with dopant levels near what we expect will work for our system, or a single gradient-doped sample of Cr:ZnSe, which would give us a continuous range of doping levels to test. Aside from reducing the overall system complexity and contributing to ruggedness, a passive Q-switch should give us the shorter pulses (on the order of 10 ns or better) desired of this laser.

6.2.2 Thermoelectric Cooler

Another immediate improvement we hope to implement is to mount the diode laser to a thermoelectric cooling plate to maintain temperature stability when the pump power is adjusted. As it stands, increasing the pump power will raise the temperature in the diode laser case, leading to a slight wavelength shift in the pump laser output. Since Tm:YAG has narrow absorption peaks, we suspect that these wavelength shifts can cause significant reductions in pump absorption, consequently creating instabilities in laser operation. By inserting the thermoelectric cooling stage between the diode case and the water cooling block, we hope to hold the diode case at a more constant temperature during power adjustments to smooth out these fluctuations.

6.2.3 Fiber Amplifier

While the first phase of this project was only concerned with generating short, spectrally-pure 2 μm pulses with no specific requirement on power, we plan to eventually scale the laser's output power up by way of a fiber amplification stage. Similar experiments have been reported in the literature by Jackson *et al.* [35] and Evgueni *et al.* [36], who were able to achieve cw output powers of 120 and 263 W, respectively. We have been lent a Tm³⁺-doped silica fiber by collaborators at the

Australian Defense Science and Technology Organisation to use for this purpose. We intend to pattern this segment of the experiment after previous work done by our lab described in [6].

6.2.4 End Mirrors

As we have discussed previously in this report, the plane-plane end mirror resonator configuration offers minimal mode confinement, rendering laser operation precarious especially at longer cavity lengths. One option we have is to replace our planar output coupler with a converging mirror, the focal length of which must be comparable to the overall cavity length. A mirror with this very short focal length that meets our transmittance requirements would likely have to be custom fabricated. Once an appropriate saturable absorber crystal is found, another option we will have is to keep the plane-plane configuration, but let the output coupler be a coating which is layered onto the face of the saturable absorber rather than having it be a separate component. The plane-plane instability would be far less prominent with this very short cavity configuration.

6.2.5 Single Frequency Operation

Ideally this laser system would run in single-frequency mode at $2.019\text{ }\mu\text{m}$, though as we have seen in section 5.4, this is not the case; there appear to be at least 14 modes oscillating in addition to the fundamental mode. There are a number of frequency-selection techniques we could utilize to reduce the number of modes, such as inserting an etalon or diffraction grating after the laser crystal, but these are likely to add considerable unwanted length to the cavity and will further raise the lasing threshold. Instead, we will make efforts to keep the cavity as short as possible by minimizing the thickness of our crystals and butting the components against each other where appropriate, which serves our primary goal of shortening pulses but also contributes to spectral purity. If we find that additional frequency filtering is needed for seeding our fiber amplifier, we can insert components between the Tm:YAG laser and the amplifier.

REFERENCES

1. T Sato, et al., 2.1- μ m-Wavelength InGaAs Multiple-Quantum-Well Distributed Feedback Lasers Grown by MOVPE Using Sb Surfactant, IEEE J. of Sel. Tops. In Q. Elec., 13, No. 5, (2007)
2. B Dickinson *et al.*, 10 mJ Output from a Gain-Switched Tm-doped Fibre Laser, Optics Communications, 182 (2000)
3. R Sharp *et al.*, 190-fs Passively Mode-Locked Thulium Fiber Laser with a Low Threshold, Optics Letters, 21, No. 12 (1996)
4. F Heine and G Huber, Tunable Single Frequency Tm:YAG Microchip Laser with External Feedback, Appl. Opt., 37, No. 15, (1998)
5. T Tsai and M Birnbaum, Q-switched 2 μ m Lasers by use of a Cr²⁺:ZnSe Saturable Absorber, Appl. Opt., 40, No. 36, (2001)
6. M Cocuzzi, Sub-Nanosecond Infrared Optical Parametric Pulse Generation in Periodically-Poled Lithium Niobate Pumped by a Seeded Amplifier, University of Dayton School of Engineering, Dayton OH (2007)
7. MJF Digonnet and WJ Miniscalco, Rare-Earth-Doped Fiber Lasers and Amplifiers, 2nd Ed., pp. 17-112, Marcel Dekker, Inc. (2001)
8. C Tiseanu, A Lupei and V Lupei, Energy Levels of Tm³⁺ in Yttrium Aluminum Garnet, J. Phys.: Condens. Matter 7 (1995)
9. A Sennaroglu and JJ Zayhowski, Solid-State Lasers and Applications, pp. 1-75, CRC Press (2007)
10. A Siegman, Lasers, University Science Books (1986)
11. G Rustad and K Stenersen, Modeling of Laser-Pumped Tm and Ho Lasers Accounting for Upconversion and Ground-State Depletion, IEEE J. of Quantum Elec., 32, No. 9 (1996)
12. B Henderson and CF Imbusch, Optical Spectroscopy of Inorganic Solids, Clarendon Press, Oxford (1989)
13. M Mond, Cr²⁺-dotierte Chalkogenide Neue Durchstimmbare Festkorperlaser und Passive Guteschalter im Mittleren Infraroten Spektralbereich, University of Hamburg Department of Physics, Hamburg, Germany (2003)
14. EC Honea, et al., 115-W Tm:YAG Diode-Pumped Solid-State Laser, IEEE J. of Quantum Elec., 33, No. 9 (1997)
15. K Lai, et al., 120-W Continuous-Wave Diode-Pumped Tm:YAG Laser, Opt. Lett., 25, No. 21 (2000)
16. L Shaw, et al., Measurement of Up-conversion Energy-transfer Probabilities in Ho:Y₃Al₅O₁₂ and Tm: Y₃Al₅O₁₂, Phys. Rev. B, 50, No. 10, (1994)
17. R Stoneman and L Esterowitz, Efficient, Broadly Tunable, Laser-Pumped Tm:YAG and Tm:YSGG CW Lasers, Opt. Lett., 15, No. 9 (1990)
18. LA Riseberg and HW Moos, Multiphonon Orbit-Lattice Relaxation of Excited States of Rare-Earth Ions in Crystals, Phys. Rev., 174 (1998)

19. Paul J. M. Suni and Sammy W. Henderson, 1-mJ/pulse Tm:YAG laser pumped by a 3-W diode laser, Opt. Lett. 16, 817-819 (1991)
20. A Kaminskii, Crystalline Lasers, CRC Press (1996)
21. W Koechner and M Bass, Solid-State Lasers, Springer-Verlag (2003)
22. R Aggarwal *et al.*, Thermo-Optic Properties of Laser Crystals in the 100-300 K Temperature Range: YAG, YALO, and YLF, Proc. of SPIE, 5707 (2005)
23. P Song, et al., Growth and Properties of Tm:YAG Crystals, J. Crystal Growth 270 (2004)
24. R Paschotta, Encyclopedia of Laser Physics and Technology, http://www.rp-photonics.com/yag_lasers.html, retrieved 3/5/2011
25. R Eng *et al.*, The Effects of Laser Phase Noise on Laser Radar Performance, Proc. of the Intl. Conf. on Lasers (1992)
26. I Melngailis *et al.*, Laser Radar Component Technology, Proc. of the IEEE, 84, No. 2 (1996)
27. N Berner *et al.*, Tm:YAG: A Comparison between Endpumped Laser Rods and the Thin Disk Setup, OSA Tops., 26, Advanced Solid-State Lasers (1999)
28. T Wagner, All Solid-State Mid-IR Laser Development, Nonlinear Absorption Investigation and Laser-Induced Damage Study, Air Force Institute of Technology, Wright Patterson Air Force Base OH (2010)
29. G Stoppler *et al.*, High-Pulse Energy Q-Switched Tm³⁺:YAG Laser for Nonlinear Frequency Conversion to the Mid-IR, Proc. of SPIE, 7836 (2010)
30. R Paschotta, Encyclopedia of Laser Physics and Technology, http://www.rp-photonics.com/thermal_lensing.html, retrieved 3/1/2011
31. A Giesen and J Speiser, Fifteen Years of Work on Thin-Disk Lasers: Results and Scaling Laws, IEEE J. of Sel. Tops. In Q. Elec., 13, No. 3 (2007)
32. R Paschotta, Encyclopedia of Laser Physics and Technology, http://www.rp-photonics.com/q_switching.html, retrieved 3/9/2011
33. PA Berry, Versatile Chromium-Doped Zinc Selenide Infrared Laser Sources, University of Dayton School of Engineering, Dayton OH (2010)
34. D Findlay and R A Clay, The Measurement of Internal Losses in 4-Level Lasers, Physics Letters, 20, No. 3 (1966)
35. S Jackson *et al.*, Application and Development of High-Power and Highly Efficient Silica-Based Fiber Lasers Operating at 2 μ m, IEEE J. of Sel. Tops. In Q. Elec., 13, No. 3 (2007)
36. S Evgueni and P Moulton, Efficient, High-Power, Tm-doped Silica Fiber Laser, conference proceedings, Advanced Solid State Photonics, Optical Society of America (2007)
37. P Peterson *et al.*, Dynamics of Passively Q-Switched Microchip Lasers, IEEE J. of Q. Elec., 35, No. 8 (1999)
38. JJ Degnan, Effects of Thermalization on Q-Switched Laser Properties, IEEE J. of Quantum Elec., 34, No. 5 (1998)

APPENDIX A – RATE EQUATION MODELING

In designing laser cavities and gain media, it is frequently useful to construct mathematical models to simulate the behavior of the system at the atomic level. This helps to predict the effects of adjusting interdependent design parameters such as pumping power, dopant concentration, cavity length etc., in both the transient and steady state cases. Laser systems are typically modeled by their rate equations, which describe the populations of all relevant atomic energy levels for the gain material, generally as a function of time. These differential equations are usually first order, or can at least be approximated to the first order, and can therefore be solved by conventional algorithms such as the Runge-Kutta method.

To model the Tm:YAG laser, the following rate equations were used, as described by Zayhowski [9] (see Table 9 for description of variables):

$$\dot{q} = \frac{2^{\ddagger} q N_{eff} \sigma_g}{t_{rt} A_g} - \frac{2_s^{\ddagger} q N_{s,g} (\sigma_{s,g} - \sigma_{s,u})}{t_{rt} A_s} - \frac{2_s^{\ddagger} q N_s \sigma_{s,u}}{t_{rt} A_s} - \frac{\gamma q}{t_{rt}} + \frac{2^{\ddagger} 2^{\dagger} N_{eff} \sigma_g}{2 t_{rt} A_g} \quad (A.1)$$

$$\dot{N}_{eff} = g_g f_g W_p (g_u f_u N_t - N_{eff}) - \frac{2^{\ddagger} 2^* q N_{eff} \sigma_g}{t_{rt} A_g} - \frac{g_u f_l N_t + N_{eff}}{\tau} \quad (A.2)$$

$$\dot{N}_{s,g} = - \frac{2_s^{\ddagger} q N_{s,g} \sigma_{s,g}}{t_{rt} A_s} + \frac{(N_s - N_{s,g})}{\tau_s} - W_{p,s} N_{s,g} \quad (A.3)$$

where q is the number of photons oscillating in the cavity, N_{eff} is the effective population inversion in the gain medium, and $N_{s,g}$ is the population of the saturable absorber ground state. The terms in each of these equations are straightforward: in the equation for photon count, the terms are (in order): stimulated emission, absorption by the Q-switch, other cavity losses, and a noise seed; in the equation for the effective population inversion: pumping, stimulated emission, and spontaneous emission; and in the equation for saturable absorber ground state population: Q-switch absorption of laser photons, spontaneous emission, and Q-switch absorption of the pump.

While there are several approximations and simplifications implicit in this description of our laser system, the most significant physical mechanisms are represented in such a way that the behavior of the model is a reasonably accurate match to the behavior of the actual system, in this case and in most others. For the sake of completeness, we will note these approximations:

With any rate equation model, it is assumed that the laser is oscillating in a single longitudinal mode. For this simple model we have assumed no cross-relaxation, though as we have mentioned in section 2.2, cross-relaxation can be a very significant process in thulium laser systems. We do not enforce conservation of population or pump depletion. Both the gain medium and the saturable absorber are approximated to two-level systems, which is to say that the lifetimes of the highest states are considered to be negligibly fast. Finally, we take thermalization of energy manifolds to be

instantaneous, though the thermalization time can become relevant if it is the same order of magnitude as the Q-switch “opening” time.

The simulation was programmed in the MATLAB software package and utilized the built-in “ode23s” Runge-Kutta differential equation solver. The following figure shows some results from the simulation. Plotted are the relative effective population inversion in the gain medium (N_{eff}), the relative population of the saturable absorber’s excited state ($N_{SA,ex}$), and the relative pulse energy (q). The time scale was chosen to show the system dynamics during the formation of a single pulse.

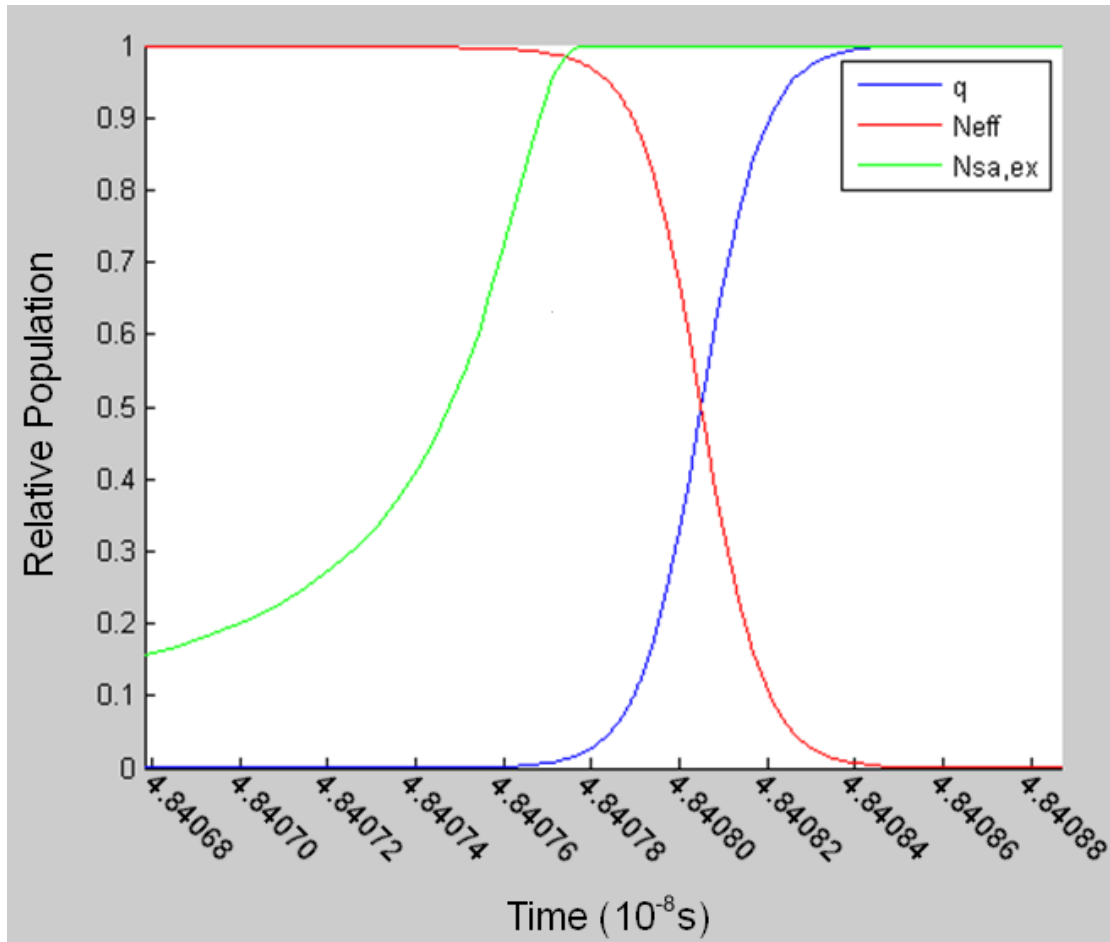


Figure 46: Relative populations of effective inversion, saturable absorber excited state, and number of photons in a laser pulse for a simulated Tm:YAG laser system. Time scale was chosen to emphasize pulse formation.

The system behaves as expected: after the saturable absorber is “bleached” (all of the population moves into the excited state, Q-switch is “open”), the population inversion in the gain medium is depleted as its energy is formed into a pulse. In the next figure, the time axis is extended:

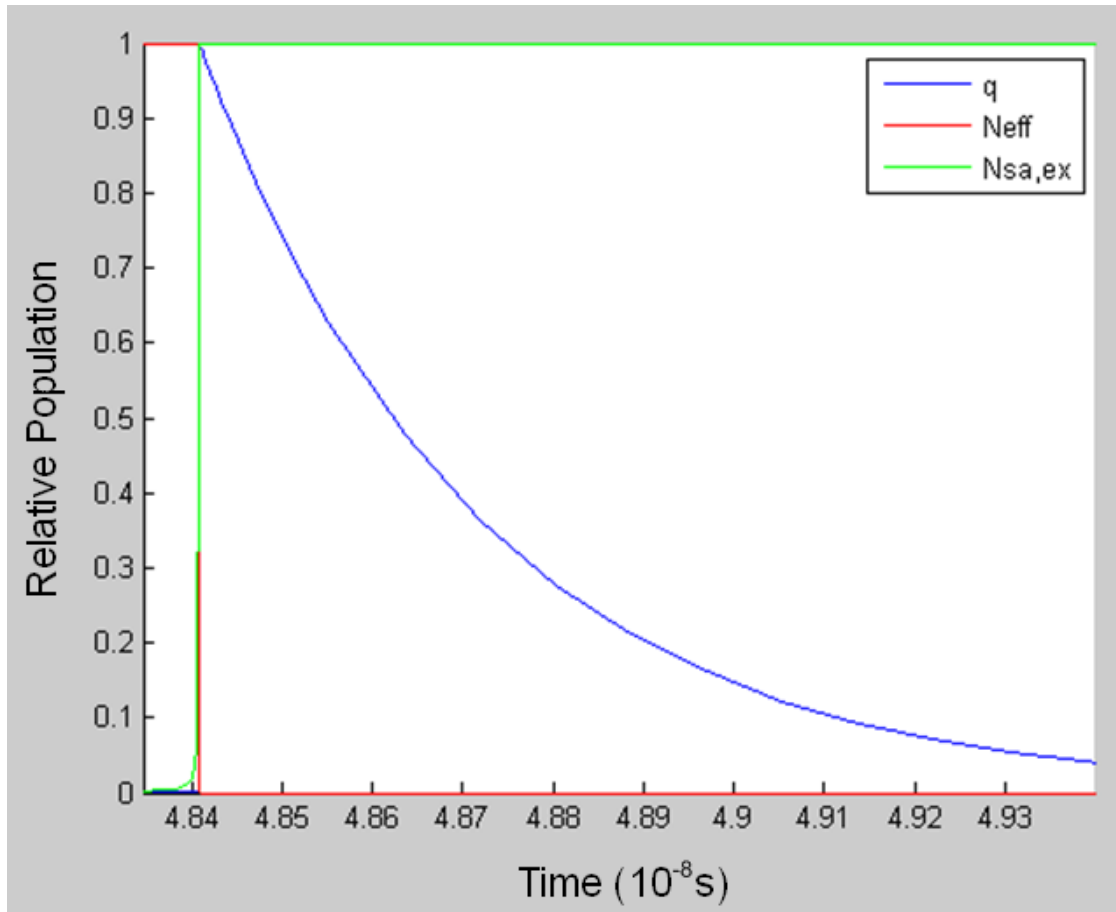


Figure 47: Relative populations of effective inversion, saturable absorber excited state, and number of photons in a laser pulse for a simulated Tm:YAG laser system. Time scale was chosen to emphasize pulse decay.

Here we see that the pulse energy decays exponentially as the pulse leaves the cavity. Again, in a qualitative sense this is the expected behavior, but a closer look reveals a significant problem: the pulse width is on the order of 1 ns when realistically it should be on the order of 10 to 100 ns. This issue was investigated extensively; system parameters were confirmed and checked against additional sources, assumptions were re-evaluated and programming was debugged. We eventually arrived at the conclusion that the fault lay with our differential equation solver. This problem is described in detail by P. Peterson *et al.* [37]: when modeling passively Q-switched laser systems, it is necessary that a differential equation solver operate within two disparate time regimes: a very short scale to deal with pulse formation, and a longer scale to deal with pulse decay. This makes the usage of a constant step size in the numerical integration very difficult, commonly leading to solver crashes or intractable computation times. The problem is exacerbated when we consider that the populations of the various energy levels can very rapidly change by ten or more orders of magnitude.

The solution is to write a custom differential equation solver capable of compensating for the idiosyncrasies inherent to this type of system. There are several general techniques that may be effective, all of which involve interrupting calculations as

the system of equations transitions between time regimes. One method is to use multiple pre-defined step sizes to be enacted as appropriate. Second, an alternate type of solver which is more suitable to a certain time regime is substituted in during the transition to that regime. Finally, and perhaps most simply, the solver can be interrupted after a pulse is completed and new initial conditions are inserted, effectively breaking a pulse train into several problems to be solved individually (this is the method proposed by Peterson).

The custom solver, while beyond the scope of this project as originally defined, is nonetheless something we plan to investigate in the future. Furthermore, rather than continue to use the simplified model described by Zayhowski [9], we intend to combine the comprehensive rate equations for Tm:YAG as defined by Rustad and Stenersen [11] with the aforementioned method of solving passively Q-switched microchip lasers as outlined by Peterson *et al.* [37] into a single program.

Table 9: Variables for Laser Modeling.

Symbol	Description
q	Number of photons in the cavity
N_{eff}	Effective population inversion
$N_{s,g}$	Population of SAQS ground state
N_t	Total absorbing gain ions
N_s	Total absorbing SAQS ions
t_{rt}	Cavity round trip time
τ	Upper state lifetime
τ_s	SAQS lifetime
f_g	Occupation probability, ground level
f_u	Occupation probability, upper laser level
f_l	Occupation probability, lower laser level
g	Degeneracy
W_p	Pump rate
A_g	Mode area in gain crystal
A_s	Mode area in SAQS
γ	Passive loss
σ_g	Stimulated emission cross-section
$\sigma_{s,g}$	Ground state absorption cross-section
$\sigma_{s,u}$	Excited state absorption cross-section in SAQS
2^{\ddagger}	Number of passes in gain medium
2_s^{\ddagger}	Number of passes in SAQS
2^{\dagger}	1 for traveling wave or 2 for standing wave
2^*	Thermalization constant

APPENDIX B – ADDITIONAL CALCULATIONS

B.1 Peak Power of a Gaussian Pulse

For a train of Gaussian pulses of known average power P_{avg} , repetition rate f , and full-width half-max pulse width τ , the pulse energy is given by [10]:

$$E_{pulse} = \int_0^\tau P_p * \text{Exp}\left(\frac{4t^2 \ln 2}{\tau^2}\right) dt \quad (\text{B.1})$$

where P_p is the peak power for the pulse. Energy per pulse for any periodic signal is equal to the average power divided by the repetition rate:

$$\frac{P_{avg}}{f} = \int_0^\tau P_p * \text{Exp}\left(\frac{4t^2 \ln 2}{\tau^2}\right) dt \quad (\text{B.2})$$

The solution to this integral comes in the form of the error function:

$$\int e^{-ax^2} dx = \frac{\sqrt{\pi} \text{erf}(\sqrt{a}x)}{2\sqrt{a}} \quad (\text{B.3})$$

Solving the above equation for the peak power gives the result:

$$P_p = \frac{P_{avg}}{\tau f} \frac{4\sqrt{\frac{\ln 2}{\pi}}}{\text{erf}(2\sqrt{\ln 2})} \quad (\text{B.4})$$

Or to approximate:

$$P_p = 1.9144 \frac{P_{avg}}{\tau f} \quad (\text{B.5})$$

B.2 Estimating Beam Quality

The beam parameter product (BPP), which is defined as the product of a beam's divergence half-angle and its radius at the waist, is a figure of merit describing how well the beam can be focused to a small spot. The BPP of an ideal Gaussian beam is given by λ/π , where λ is the beam's wavelength. A second quantity, M^2 , also called the Gaussian beam parameter, is defined as the ratio of a measured BPP to an ideal BPP at that wavelength. To estimate the M^2 of our pump diodes for simulation purposes, we take the beam waist to be the core diameter of the fiber, while the divergence angle is calculated from the fiber's numerical aperture. For the Bright Solutions pump laser:

$$M^2 = \frac{r_0 \theta \pi}{\lambda} \quad (\text{B.6})$$

where:

$$\begin{aligned}\lambda &= 785 \text{ nm} \\ \theta &= 0.22 \text{ rad} \\ r_0 &= 100 \text{ }\mu\text{m}\end{aligned}$$

which gives us $M^2 = 88$.

B.3 Calculating Absorption Coefficient for Tm:YAG

It is necessary for us to know exactly how much pump power is being absorbed by the gain crystal so we know what to expect for laser operation. Based on data collected with our Cary 5000 spectrophotometer on Tm:YAG spectroscopic crystals, we calculate the absorption coefficient:

The measured absorbance 'A' for an uncoated, 1mm-thick, 6% doped spectroscopic sample of Tm:YAG was 0.273:

$$A = -\log(T) \quad (B.7)$$

So the total transmittance for the crystal is 53.33%. The refractive index of YAG at the pump wavelength is 1.83, so the power reflection loss at a single interface is:

$$R = \left(\frac{n_1 - n_2}{n_1 + n_2} \right)^2 = 8.6\% \quad (B.8)$$

So the transmittance at each interface is 91.4%. If we approximate the total Fresnel reflection losses to the single pass losses, the total transmittance is the transmittance of the medium itself multiplied with the Fresnel transmittance for two interfaces:

$$T_m * (0.914)^2 = 53.33\% \quad (B.9)$$

$$T_m = 63.84 \quad (B.10)$$

Now we can use Beer's Law to calculate the absorption coefficient α for the Tm:YAG. L is the length of the crystal:

$$T_m = \exp(-\alpha L) \quad (B.11)$$

$$63.84\% = \exp(-\alpha[0.1 \text{ cm}]) \quad (B.12)$$

$$\alpha = 4.488 \text{ cm}^{-1} \quad (B.13)$$

To convert this to an approximate absorption cross-section, we apply the relationship:

$$\alpha = \sigma_{abs} \quad (B.14)$$

where N is the density of Tm^{3+} ions in the host material and was calculated to be $8.3 * 10^{20} \text{ cm}^{-3}$. This yields the result of:

$$\sigma_{abs} = 5.4 * 10^{-21} \text{ cm}^2 \quad (B.15)$$

B.4 Absorption with Compensation for Fresnel Reflectance

From our collected absorption spectrum (see section 2.5), it is clear that our absorbance (or optical density) at a pump wavelength of 785 nm is 0.26. However, this does not account for losses due to Fresnel reflection. Converting optical density to transmittance:

$$T = 10^{-OD} \quad (B.16)$$

gives us a value of $T = 55\%$. If we calculate the normal-incidence Fresnel reflections assuming YAG's index of refraction is 1.82:

$$R = \left(\frac{n_1 - n_2}{n_1 + n_2} \right)^2 \quad (B.17)$$

we get a reflectance of 8.5% per interface, or approximately 17% total. This means that 48% of the beam was absorbed by the crystal.

APPENDIX C – MATLAB CODE

C.1 Cr:ZnSe/Cr:ZnS Passive Q-Switch Model

```
clear all
close all
clc

%designate a vector of pump powers (in log space)
P = logspace(-5,10,500); %pump power (W)
%designate a vector for transmittances
T = zeros(length(P),1);

for j=1:length(P)

    %crystal specs (cr:znse)
    nt = 5e24; %total carrier density (m^-3)
    Sabs = 6e-23; %absorption cross section (m^2)
    Sem = 3e-23; %emission cross section (m^2)
    L = 250e-6; %length of crystal (m)
    t = 4e-6; %upper state lifetime (s)

    % %crystal specs (cr:znns)
    % nt = 1e24; %total carrier density (m^-3) [2]
    % Sabs = 1.32e-23; %absorption cross section (m^2) [1]
    % Sem = 11.07e-23; %emission cross section (m^2) [1]
    % L = 2e-3; %length of crystal (m)
    % t = 4.25e-6; %upper state lifetime (s) [1]

    %sources
    %[1] sorokina, sorokin, mirov, et al, appl phys b 2002
    %[2] in-house

    %other specs
    WL = 2000e-9; %wavelength (m)
    Pin = P(j); %incident power (W)
    d = 1e-3; %spot diameter (m)
    Iin = Pin/(pi*(d/2)^2); %incident intensity (W/m^2)
    EeV = (1240e-9)/WL; %photon energy (eV)
    E = EeV*1.602e-19; %photon energy (J)

    steps = 1000; %number of steps to solve for
    dz = L/steps; %length element
    z = linspace(0,L,steps); %length vector (m)

    I = zeros(1,length(z)); %intensity vector
    I(1) = Iin;
    n = zeros(1,length(z)); %upper state population vector
    n(1) = (nt*Sabs)/((Sabs+Sem)+E/(Iin*t));

    for i = 2:length(z)
        n(i) = (nt*Sabs)/((Sabs+Sem)+E/(I(i-1)*t));
        dI = I(i-1)*(n(i)*(Sem+Sabs)-Sabs*nt)*dz;
```

```

        I(i) = I(i-1)+dI;
        clear dI;
    end

    %calculate transmittance
    T(j) = I(length(I))/I(1);

    clear i

end

%incident intensity vector
Iplot = P./((pi*(d/2)^2)*1e4);

%plot transmittance vs incident power
semilogx(Iplot,T)
xlabel('Input Intensity (W/cm ^2)')
ylabel('Transmittance (%)')

```

C.2 Tm:YAG Laser Model – Parameter Definitions

```

%{
NOTES:
- Mode volumes are approximated to be cylindrical in short cavities
- In the rate eqs I have substituted Neff for Nu in the spontaneous emission
term, based on Senn. p. 13
- Degeneracy is ignored
%}

clear all
close all

%make variables global so D Eq function can see them
global X Xs Xt X2 rtt SgEm SsAbs SsAbsE As Ag Grt Ns Ng fu fl fg Wp tg ts Wps

%design parameters
Pp = 40; %pump power, W
Lp = 785; %pump wavelength, nm

Lg = .025; %length of gain crystal, cm
Ls = .1; %length of saturable absorber, cm
Ld = .001; %length of gap between crystals, cm

SAdoping = .001; %percent doping (atomic) in saturable absorber
GMdoping = .06; %percent doping (atomic) in gain medium

dg = .005; %mode diameter in gain crystal, cm
ds = .005; %mode diameter in saturable absorber, cm

X = 2; %number of passes 2^++, 2 or 1
X2 = 2; %2^+, 1 for traveling wave or 2 for standing, only used in
spontaneous emission term

```

```

Xs = 2; %number of passes in saturable absorber 2s^++, 2 or 1

Roc = 0.7; %output coupler reflectance

%known values
c = 3e10; %c in cm/s
hc = 1240; %hc in eV*nm
eVinJ = 1.602e-19; %eV in a J

ng = 1.833; %index of YAG at 785 nm
ns = 2.67; %index of ZnSe at 785 nm

fu = 1; %manifold occupation probability of upper laser level
fl = .5; %manifold occupation probability of lower laser level
fg = .5; %manifold occupation probability of ground level
Xt = fu+fl; %thermalization constant 2*, ranges from 1 to 2, see Sennaroglu
p. 17

SgAbs = 4.8e-21; %absorption cross-section of gain crystal, cm^2
SgEm = 2.2e-21; %emission cross-section of gain crystal, cm^2
SsEm = 1.5e-19; %emission cross-section of saturable absorber
(excited@laser), taken from mond fig. 5.10, cm^2
SsAbs = 6e-19; %absorption cross-section of saturable absorber
(ground@laser), taken from mond fig. 5.10, cm^2
SsAbsE = 0; %absorption cross-section of saturable absorber (excited@laser);
pat says this is 0 for Cr:ZnSe
SsAbsP = 0; %absorption cross-section of saturable absorber (ground@pump);
this is probably 0 for Cr:ZnSe

Nz = 2.1963e022; %number of Zinc ions in ZnSe, cm-3
Ny = 1.3869e022; %number of Y ions in YAG, cm-3

ts = 6e-6; %upper state lifetime of saturable absorber, s
tg = 11e-3; %lifetime of upper laser level (tau), s

Gcav = .05; %RT absorption/scattering loss

%calculated values
rtt = 2*( (Lg*ng)/c + (Ls*ns)/c + Ld/c ); %round trip time in cm/s

Ag = (dg/2)^2 * pi; %mode area in gain crystal, cm^2
As = (ds/2)^2 * pi; %mode area in saturable absorber, cm^2
Vg = Ag*Lg; %estimate of mode volume in gain crystal, cm^3
Vs = As*Ls; %estimate of mode volume in saturable absorber, cm^3

Ds = Nz*SAdoping; %density of saturable absorber ions, cm^-3
Ns = Ds*Vs; %total saturable absorber ions in mode volume
Dg = Ny*GMdoping; %density of gain ions, cm^-3
Ng = Dg*Vg; %total gain ions in mode volume

AbsEff = 1-exp(-SgAbs*X*Lg*Dg); %Beer's law absorption efficiency of pump by
gain medium (double pass)

```

```

AbsEffs = 1-exp(-SsAbsP*Xs*Ls*Ds); %Beer's law absorption efficiency of pump
by saturable absorber (double pass)

Ep = (hc/Lp)*eVinJ; %energy of a pump photon, J
Qps = Pp/Ep; %incident pump photons per second
Ips = Pp/As; %pump intensity in saturable absorber, W/cm^2
Ipsat = Ep/(ts*SsAbsP); %saturation intensity in saturable absorber, W/cm^2

Wp = AbsEff*Qps; %pump rate, # of absorbers per second
Wps = AbsEffs*Qps; %pump rate, # of absorbers per second (saturable absorber)

Grt = Gcav + (1-Roc); %round trip loss incl. OC

%initial conditions
%q0 = 0; %number of photons in the cavity
q0 = 1;
Nsg0 = (Ds*Vs)/(1+Ips/Ipsat); %ground state of saturable absorber (eq 3)
%Neff0 = (Ag/(X*SgEm))*((Xs*Nsg0*As^-1*(SsAbs-SsAbsE))+(Xs*Ns*SsAbsE*As^-
1)+Grt); %effective population inversion
Neff0 = Ng;

initconds = [q0 Neff0 Nsg0];

%call rate equations
maxtime = .0001; %in seconds
options = odeset('MaxStep',1e-7);
[T,N] = ode23s(@zay_model2,[0 maxtime],initconds,options);

%plotting
%subplot is (rows, columns, position)
subplot(3,1,1);
plot(T,N(:,1))
legend('q')

subplot(3,1,2);
plot(T,N(:,2))
legend('Neff')

subplot(3,1,3);
plot(T,N(:,3))
legend('Nsg')

figure
hold on

plot(T,N(:,1)./max(N(:,1)), 'b')
plot(T,N(:,2)./max(N(:,2)), 'r')
plot(T,(Ns-N(:,3))./Ns, 'g')
legend('q', 'Neff', 'Nsa,ex')

hold off

```

C.3 Tm:YAG Laser Model – Differential Equation Solver

```
function dn = zay_model2(t,n)

global X Xs Xt X2 rtt SgEm SsAbs SsAbsE As Ag Grt Ns Ng fu fl fg Wp tg ts Wps

%rate equations
dn = zeros(3,1);

%all of the following are counts, not ratios

%dq/dt, photon count
dn(1) = (n(1)/rtt) * ... %multiplicative factor
    ( X*SgEm*n(2)*Ag^-1 ... %laser photon emission
    - Xs*(SsAbs-SsAbsE)*n(3)*As^-1 ... %ground state SA absorption
    - Xs*Ns*SsAbsE*As^-1 ... %excited state SA absorption, approx. 0
    - Grt) ... %cavity losses
    + (X*X2*n(2)*SgEm)/(2*Ag*rtt); %noise seed

%dNeff/dt, effective inversion
dn(2) = -Xt*X*SgEm*n(1)*n(2)*rtt^-1*Ag^-1 ... %laser photon emission
    - (fl*Ng+n(2))/tg ... %spontaneous emission
    + fg*Wp*(fu*Ng-n(2)); %pump absorption

%dNs/dt, saturable absorber ground state
dn(3) = -Xs*SsAbs*n(1)*n(3)*rtt^-1*As^-1 ... %absorption of laser photons
    + (Ns-n(3))/ts ... %spontaneous emission
    - Wps*n(3); %absorption of pump, approx. 0
```